

1 *Research article*

2 **Automated riverbed composition analysis using Deep Learning** 3 **on underwater images**

4 Alexander A. Ermilov¹, Gergely Benkő¹ and Sándor Baranya¹

5 ¹Department of Hydraulic and Water Resources Engineering, Budapest University of Technology and Economics,
6 Budapest, 1111, Hungary

7 *Correspondence to:* Alexander A. Ermilov (ermilov.alexander@emk.bme.hu)

8 **Abstract.** The sediment of alluvial riverbeds plays a significant role in river systems both in engineering and
9 natural processes. However, the sediment composition can show great spatial and temporal heterogeneity, even
10 on river reach scale, making it difficult to representatively sample and assess. Conventional sampling methods in
11 such cases cannot describe well the variability of the bed surface texture due to the amount of energy and time
12 they would require. In this manuscript, an attempt is made to overcome this issue by introducing a novel image-
13 based, Deep Learning (DL) algorithm and related field measurement methodology with potential for becoming a
14 complementary technique for bed material samplings and significantly reducing the necessary resources. The
15 algorithm was trained to recognise main sediment classes in videos that were taken underwater in a large river
16 with mixed bed sediments, along cross-sections, using In total, 27 physical bedmaterial samples were collected
17 and sieved for the validation purposes. The introduced DL-based method is fast, i.e., the videos of 300-400-meter-
18 long sections can be analysed within minutes, with very dense spatial sampling distribution. The goodness of the
19 trained algorithm was evaluated i) mathematically by dividing the annotated images into test and validation sets,
20 and also via ii) intercomparison with other direct (sieving of physical samples) and indirect sampling methods
21 (wavelet-based image processing of the riverbed images), focusing on the percentages of the detected sediment
22 fractions. For the final evaluation, the sieving analysis of the collected physical samples were considered as the
23 ground truth. This meant a total of 27 measurement points, where the DL-results could be compared with the two
24 other methods. During data processing, outlier points, where the collected physical samples did not represent the
25 riverbed surface images taken there (e.g., due to bedarmour), were removed. In the remaining 14 points, the DL
26 algorithm produced promising results with a mean error of 4.5%. Besides, the spatial trend in the fraction changes
27 was also well captured along the cross-sections, based upon the visual evaluation of the footages. Furthermore,
28 comparison with the wavelet-based image processing justified the selection of the outlier points earlier, as its
29 results matched closely with the DL detections in these purely gravel-covered points and showed no sign of finer
30 fractions, univocally opposing the content of the physical samples. Suggestions for performing proper field
31 measurements are also given, furthermore, possibilities for combining the algorithm with other techniques are
32 highlighted, briefly showcasing the multi-purpose of underwater videos for hydromorphological assessment.

33 **Keywords:** riverbed texture, underwater mapping, sediment classes, Artificial Intelligence, Deep Learning,
34 image-based

35 **1 Introduction**

36 The physical composition of a riverbed plays a crucial role in fluvial hydromorphological processes, as a sort of
37 boundary condition in the interaction mechanisms between the flow and the solid bed. Within these processes, the

38 grains on the riverbed are responsible for multiple phenomena, such as flow resistance (Vanoni and Hwang, 1967;
39 Zhou et al., 2021), stability of the riverbed (Staudt et al., 2018; Obodovskyi et al., 2020), development of bed
40 armour (Rákóczi, 1987; Ferdowsi et al., 2017), sediment clogging (Rákóczi, 1997; Fetzer et al., 2017), fish shelter
41 (Scheder et al., 2015), etc. Through these physical processes, the bed material composition has a determining
42 effect on numerous river-uses, e.g., possibilities of inland waterway transport (Xiao et al., 2021), drinking water
43 supply through bank filtration (Cui et al., 2021), or the quality of riverine habitats (Muñoz-Mas et al., 2019)..
44 Knowledge of riverbed morphology and sediment composition (sand, gravel and cobble content) is therefore of
45 major importance in river hydromorphology. In order to gain information about riverbed sediments, in situ field
46 sampling methodologies are implemented.

47

48 Traditionally, bed material sampling methods are intrusive (i.e., sediment is physically extracted from the bed for
49 follow-up analysis) and carried out via collecting the sediment grains one-by-one (areal, grid-by-number and
50 pebble count methods, see e.g., Bunte and Abt, 2001; Guerit et al., 2018) or in a larger amount by a variety of
51 grab samplers (volumetric methods, such as WMO, 1981; Singer, 2008). This is then followed by measuring their
52 sizes individually on-site or transporting them to a laboratory for mass-sieving analysis (Fehr, 1987; Diplas, 1988;
53 Bunte and Abt, 2001). These sampling procedures are time- and energy consuming, especially in large gravel and
54 mixed bed rivers, where characteristic grain sizes can strongly vary both in time and space (Wolcott and Church,
55 1991; USDA, 2007), requiring a dense sampling point allocation. The same goes for critical river reaches, where
56 significant human impact led to severe changes in the morphological state of the rivers (e.g., the Upper section of
57 the Hungarian Danube; Török and Baranya, 2017). When assessing bed material composition on a river reach
58 scale, experts usually try to extrapolate from the samples, and describe larger regions of the bed (even several
59 thousand m²) by data gathered in a few, several dozen points (see e.g., USDA, 2007; Haddadchi et al., 2018;
60 Baranya et al., 2018; Sun et al., 2021). Gaining a representative amount of the sediment samples is also a critical
61 issue. For instance, following statistical criteria such as those of Kellerhals and Bray (1971) or Adams (1979), a
62 representative sample should weigh ten-to-hundred kg. Additionally, physical bed material sampling methods are
63 unable to directly quantify important, hydromorphological features such as roughness or bedforms (Graham et al.,
64 2005). Due to these constraints, surrogate approaches have recently been intensively tested to analyse the riverbed.
65 Major examples are introduced in the rest of this section.. Unlike the conventional methods, these techniques are
66 non-intrusive and rely on computers and other instrumentation to decrease the need of human intervention and
67 speed up the analyses.

68

69 One group of the surrogate approaches is the acoustic methods, where an acoustic wave source (e.g., an Acoustic
70 Doppler Current Profiler; ADCP) is pointed towards the riverbed from a moving vessel, emitting a signal. The
71 strength and frequency of this signal is measured while it passes through the water column, reflecting back to the
72 receiver from the sediment transported by the river, and finally from the riverbed itself. This approach is fast and
73 larger areas can be covered relatively quickly (Grams et al., 2013). While it has already become widely used for
74 describing sediment movement (i.e., suspended sediment, Guerrero et al., 2016; bedload, Muste et al., 2016; and
75 indirectly flow velocity; Shields and Rigby, 2005) and channel shape (Zhang et al., 2008), it has not reached
76 similar breakthrough for riverbed material analysis. Researchers experimented with the reflecting signal strength
77 [dB] from the riverbed (e.g., Shields, 2010) to establish its relationship with the riverbed material. Their hypothesis

78 was that the absorption (and hence the reflectance) of the acoustic waves reaching the bed correlates with the type
79 of bed sediment. Following initial successes, the method presented several disadvantages and limitations, hence
80 it could not establish itself as surrogate method for riverbed material measurements so far. For example, Shields
81 (2010) showed that it was necessary to apply instrument specific coefficients to convert the signal strength into
82 bed hardness, and these coefficients could only be derived by first validating each instrument using collected
83 sediment samples with corresponding ADCP data. Moreover, the method was sensitive to the bulk density of the
84 sediment and to bedforms. Based on his results and observations, the sediment classification could only extend to
85 differentiate between cohesive (clay, silt) and non-cohesive (sand, gravel) sediment patches, but gravel could not
86 be distinguished strongly from sand as they produced similar backscatter strengths. Buscombe et al. (2014a;
87 2014b) further elaborated on the topic and successfully developed a better, less limited, decision tree-based
88 approach. They showed that spectral analysis of the backscatter is much more effective for differentiating the
89 sediment types compared to the statistical analysis used by Shields. With this approach it became possible to
90 classify homogenous sand, gravel, and cobble patches. However, Buscombe et al. (2014a, 2014b) also emphasizes
91 that acoustic approaches are not capable of separating the effects of surface roughness from the effects of
92 bedforms, therefore the selection of an appropriate ensemble averaging window size is of great importance for
93 their introduced method. This size should be small enough to not include morphological signal, for which
94 however, the a priori analyses of riverbed elevation profiles is needed at each site. Furthermore, they suggest their
95 method is sensitive to and limited by high concentrations of (especially cohesive) sediment, therefore its
96 application to heterogeneous riverbeds would require site specific calibrations. The above-mentioned studies also
97 note that acoustic methods in general inherently do not allow the measurement of individual sediment grains due
98 to their spatial averaging nature. The detected signal strength correlates with the median grainsize of the covered
99 area, information about other nominal grain sizes cannot be gained.

100
101 Another group of the surrogate approaches is the application of photography (Adams, 1979; Ibbekken and
102 Schleyer, 1986) and later computer vision or image-processing techniques. During the last two decades, two major
103 subgroups emerged: one uses object- and edge detection (by finding abrupt changes in intensity and brightness of
104 the image, segmenting objects from each other; Sime and Ferguson, 2003; Detert and Weitbrecht, 2013), and the
105 other one analyses the textural properties of the whole image, using autocorrelation and semi-variance methods
106 to define empirical relationship between image texture and the grain sizes of the photographed sediments (Rubin,
107 2004; Verdú et al., 2005). Both image processing approaches were very time consuming and required mostly site-
108 specific manual settings, however, a few transferable and more automated techniques have also been developed
109 recently (e.g., Graham et al., 2005; Buscombe, 2013). Even though there is a continuous improvement in the
110 applied image-based bed sediment analysis methods, there are still major limitations the users face with, such as:

- 111
112 • Most of the studies (all the ones listed above) focuses on gravel bed rivers, and only a few exceptions
113 can be found in the literature where sand is also accounted for (texture-based methods; e.g.:
114 Buscombe, 2013).
- 115 • The adaptation environment was typically non-submerged sediment, instead of underwater
116 conditions (a few exceptions: Chezar and Rubin, 2004; Warrick et al., 2009).

- 117 • The computational demand of the image processing is high (e.g., one to ten minutes per image;
118 Detert and Weitbrecht, 2013).
- 119 • The analysis requires operator expertise (higher than in case of any conventional method).
- 120 • There is an inherent pixel- and image resolution limit (Buscombe and Masselink, 2008 Cheng, 2015;
121 Purinton and Bookhagen, 2019). The finer the sediment, the higher resolution of the images should
122 be (higher calculation time), or they must be taken from a closer position (smaller area and sample
123 per image).

124

125 Nowadays, with the rising popularity of Artificial Intelligence (AI), several Machine Learning (ML) techniques
126 have been implemented in image recognition as well. The main approaches of segmentation contra textural
127 analysis still remain; however, an AI defines the empirical relationship between the object sizes (Ighathinatane et
128 al., 2009; Kim et al., 2020) or texture types (Buscombe and Ritchie, 2018) in the images and their real sizes. In
129 the field of river sedimentology a few examples can already be found, where ML (e.g., Deep Learning; DL) was
130 implemented. For instance, Rozniak et al. (2019) developed an algorithm for gravel-bed rivers, performing
131 textural analysis. With this approach, information is not gained on individual grains (e.g., their individual shape
132 and position), but rather the general grain size distribution (GSD) of the whole images. At certain points of the
133 studied river basins, conventional physical samplings (pebble count) were performed to provide real GSD
134 information. Using this data, the algorithm was trained (with ~1000 images) to estimate GSD for the rest of the
135 study site, based on the images. The method worked for areas where grain diameters were larger than 5 mm, and
136 the sediment was well-sorted. The developed method showed sensitivity to sand coverage, blurs, reduced
137 illuminations (e.g., shadows) and white pixels. Soloy et al. (2020) presented an algorithm which used object
138 detection on gravel- and cobble covered beaches to calculate individual grain sizes and shapes. 46 images were
139 used for the model training, however, the number of images were multiplied with data augmentation (rotating,
140 cropping, blurring the images; see Perez and Wang, 2017) to enhance the learning session and increase the input
141 data. The method was able to reach a limited execution speed of a few seconds per m² and adequately measured
142 the sizes of gravels. Ren et al. (2020) applied an ensemble bagging-based Machine Learning (ML) algorithm to
143 estimate GSD along the 70 km long Hanford Reach of the Columbia River. Due to its economic importance, a
144 large amount of measurement data has been accumulated for this study site over the years, making it ideal for
145 using ML. By the time of the study, 13,372 scaled images (i.e., their millimetre/pixel ratio was known) were taken
146 both underwater and in the dry zones, covering approx. 1 m² area each. The distance between the image-sampling
147 points was generally between 50-70 m. An expert defined the GSD (8 sediment classes) of each image by using a
148 special, visual evaluation-classification methodology (DeLong and Brusven, 1991; Geist et al., 2000). This dataset
149 was fed to a ML algorithm along with their corresponding bathymetric attributes and hydrodynamic properties,
150 simulated with a 2D hydrodynamic model. Then, it was tested to predict the sediment classes based on the
151 hydrodynamic parameters only. The algorithm performed with a mean accuracy of 53%. Even though this method
152 was not image-based (only indirectly, via the origin of the GSD data), it highlighted the possibilities of an AI for
153 a predictive model, using a high-dimensional dataset. Having such a large data of grain size information can be
154 considered exceptional and takes a huge amount of time to gather, even with the visual classification approach
155 they adapted. Moreover, this was still considered spatially sparse information (point-like measurements, 1 m²
156 covered area/image dozens of meters away from each other). Buscombe (2020) used a set of 400 scaled images

157 to train an AI algorithm on image texture properties, using another image-processing method (Barnard et al., 2007)
158 for validation. The algorithm reached a good result for not only gravel, but sand GSD calculation as well,
159 outperforming an earlier, but promising, texture-based method (wavelet analysis; Buscombe, 2013). In addition,
160 the method required fewer calibration parameters than the wavelet image-processing approach. The study also
161 foresaw the possibility to train an AI which estimates the real sizes of the grains, without knowing the scale of
162 one pixel (mm/pixel ratio) if the training is done properly. The AI might learn unknown relationships between the
163 texture and sizes if it is provided with a wide variety (images of several sediment classes) and scale (mm/pixel
164 ratio)) of dataset (however, it is also prone to learn unwanted biases). Recently, Takechi et al. (2021) further
165 elaborated on the importance of shadow- detection and removal, using a dataset of 500 pictures for training a
166 texture-based AI, with the help of an object-detecting image-processing technique (Basegrain; Detert and
167 Weitbrecht, 2013). The previously presented studies, applying ML and DL techniques, significantly contributed
168 to the development and improvement of surrogate sampling methods, incorporating the great potential in AI.
169 However, there are still several shortcomings to these procedures. Firstly, none of the image-based AI studies
170 used underwater recordings, even though the underwater environment offers completely different challenges.
171 Secondly, the training images were always scaled, i.e., the sizes of the grains could be easily reconstructed, which
172 is again complicated to accomplish in a river. Lastly, they were not adapted for continuous (i.e., spatially dense)
173 measurement, but rather focused on a sparse grid-like approach.

174

175 The goal of this manuscript is to further investigate the applicability of image processing as a surrogate method,
176 and attempt to break through or go around the above mentioned shortcomings of the AI-based approaches. Hence,
177 we introduce a riverbed material analysing, Deep Learning (DL) algorithm and field measurement methodology,
178 along with our first set of results. The introduced technique can be used to measure the gravel and sand content of
179 the submerged riverbed surface. It aims to eventually become a practical tool for exploratory mapping, by
180 detecting sedimentation features (e.g., deposition zones of fine sediment, colmation zones, bed armour) and
181 helping decision making for river sedimentation management. Also, the long-term hypothesis of the authors
182 includes the creation of an image-based measurement methodology, where underwater videos of the riverbed
183 could serve multiple sediment related purposes simultaneously. Part of which is the current approach for mapping
184 the riverbed material texture and composition. Others include measuring the surface roughness of the bed (Ermilov
185 et al., 2020) and detecting bedload movement (Ermilov et al., 2022).

186

187 Compared to the studies introduced earlier, the main novelty of our manuscript is that both the training and
188 analysed videos are recorded underwater, continuously along cross-sections of a large river. Furthermore, the
189 training is unscaled, i.e., the camera-riverbed distance could vary while recording the videos, without considering
190 image-scale. Moreover, compared to the relatively low number of training images in most of the above referred
191 studies, we used a very large dataset (~15000) of sediment images for the texture-based AI, containing mostly
192 sand, gravel, cobble, and to a smaller extent: bedrock together with some other, non-sediment related objects.

193

194 **2 Methods**

195 **2.1 Case studies**

196 The results presented in this study are based on riverbed videos taken during three measurement campaigns, in
197 sections of the Danube River, Hungary. The first campaign was at Site A, Ercsi settlement (~ 1606 rkm) where 3
198 transects were recorded, the second one was at Site B, Gönyű settlement (~ 1791 rkm) with 2 transects, and the
199 third was at Site C, near to Göd settlement (~ 1667 rkm) with 2 transects (Fig. 1). Each transect was recorded
200 separately (one video per transect), therefore our dataset included a total of 8 videos.



201 **Figure 1: The location of the riverbed videos, where the underwater recordings took place. All sites were located in**
202 **Hungary, Central Europe. The surveys were carried out on the Danube River, Hungary’s largest river.**
203

204 The training of the DL algorithm was done using the video images of Site C and a portion of A (test set; see later
205 in Section 2.3), while Site B and the rest of the images from A served for validation. The measurements were
206 carried out during daytime, at mid-water regime ($Q = 1900 \text{ m}^3/\text{s}$) in case of Site A, and low water regime ($Q =$
207 $1350 \text{ m}^3/\text{s}$) at Site B, and Site C ($Q = 700 \text{ m}^3/\text{s}$). This latter site served only for increasing the training image
208 dataset (i.e., conventional samplings were not carried out at the time of recording the videos), thus we do not go
209 into further details with it for the rest of the manuscript, but the main characteristics are listed in Table 1.

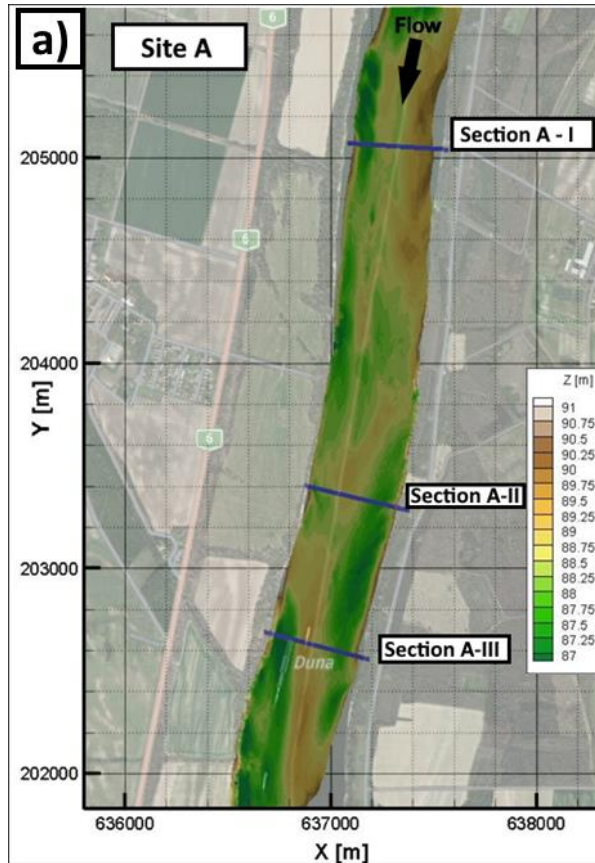
210

	Site A	Site B	Site C
$Q_{\text{survey}} [\text{m}^3/\text{s}]$	1900	1350	700
$B_{\text{survey}} [\text{m}]$	300 – 450		
$H_{\text{mean, survey}} [\text{m}]$	3.5 - 4.5		
$S_{\text{survey}} [\text{cm}/\text{km}]$	15		
$SSC_{\text{survey}} [\text{mg}/\text{l}]$	25	20	14

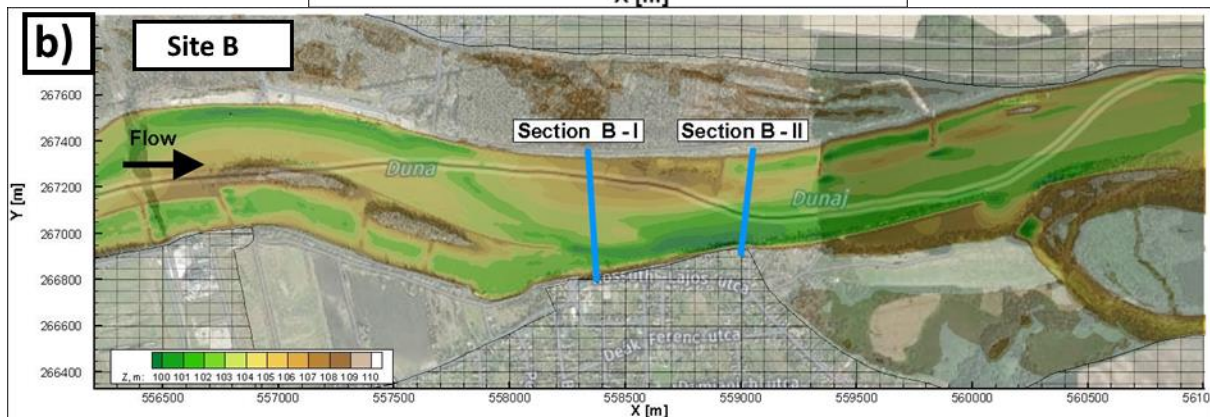
Characteristic sediment	riverbed	gravel, sandy gravel	gravel, gravelly sand	gravel, sandy gravel
Q_{annual,mean} [m³/s]		2000	2200	1400
Q_{1%} [m³/s]		5300	5500	4700

211 **Table 1: Main hydromorphological parameters of the measurement sites. Q_{survey}: discharge during survey; B_{survey}: river**
212 **width during survey; H_{mean,survey}: mean water depth during the survey; S_{survey}: riverbed slope during survey; SSC_{survey}:**
213 **mean suspended sediment concentration during the survey; Q_{annual, mean.}: annual-mean of the discharge at the site; Q_{1%}:**
214 **discharge of 1% probability.**

215 As underwater visibility conditions are influenced by the suspended sediment (SSC_{survey} – susp. sed.
216 concentration), the characteristics of this sediment transport is also included in Table 1. The highest water depths
217 were around 6-7 m in all cases. In Site A, measurements included mapping of the riverbed with a camera along
218 three separate transects (Fig. 2a). At Site B, two transects were recorded (Fig. 2b).



219



220

221

222

223

Figure 2: Bathymetry of Site A and B. The measurement cross-sections are also marked. The vessel moved along these lines from one bank to the other, while carrying out ADCP measurement and recording riverbed videos. Physical bed material samples were also collected in certain points of these sections.

224

225 2.2 Field data collection

226

227

228

229

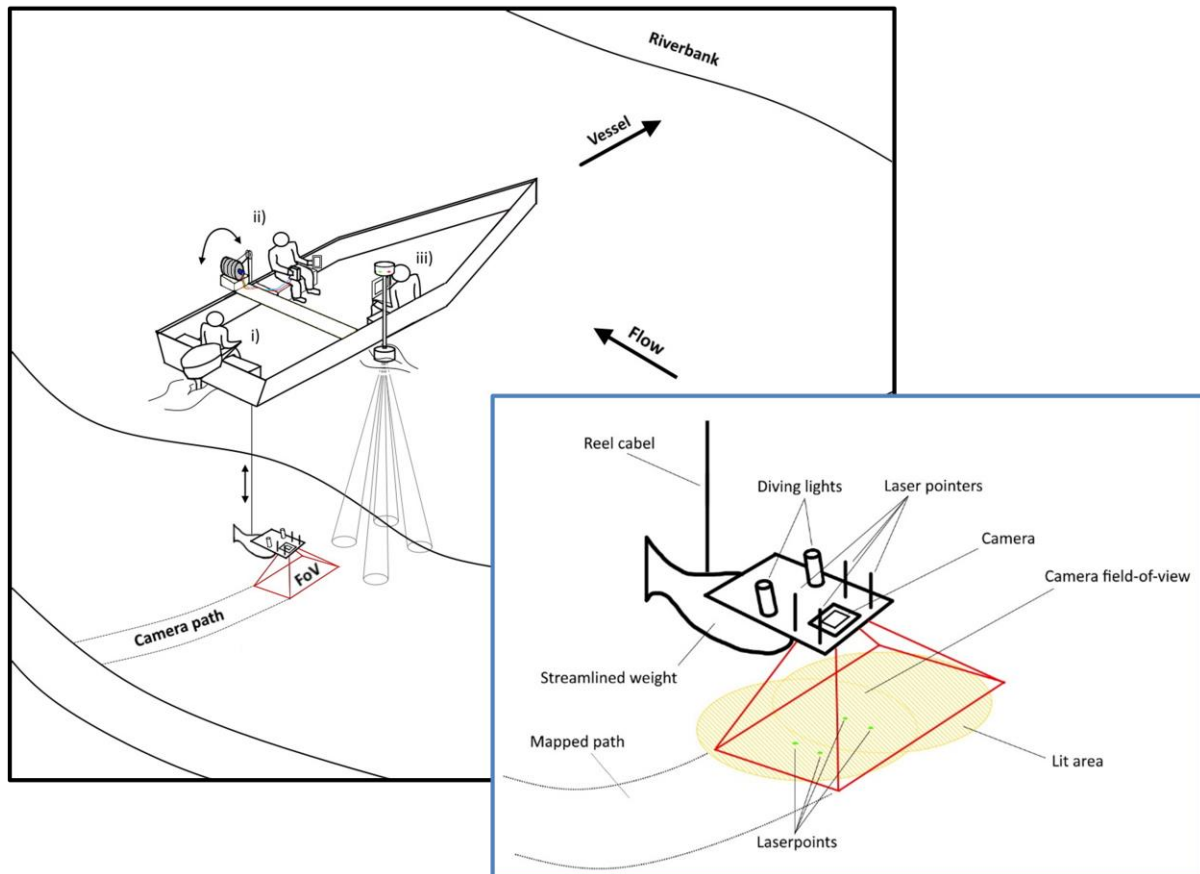
230

231

232

Fig. 3 presents a sketch of the measurement process with the equipment and a close-up of the underwater instrumentation. During the field measurements, the camera was attached to a streamlined weight (originally used as an isokinetic suspended sediment sampler) and lowered into the water from the vessel by an electric reel. The camera was positioned perpendicularly to the water and the riverbed, in front of the nose of the weight. Next to the camera, two diving lights worked as underwater light sources, focusing into the camera's field of view (FoV). In addition, four laser pointers were also equipped in hand-made isolation cases to provide possible scales for secondary measurements. They were also perpendicular to the bottom, projecting their points onto the underwater

233 camera field of view. Their purpose was to ensure a visible scale (mm/pixel ratio) in the video footages for
234 validation. During the measurement procedure, a vessel crossed the river slowly through river transects, while the
235 position of the above detailed equipment was constantly adjusted by the reel. Simultaneously, ADCP and RTK
236 GPS measurement were carried out by the same vessel, providing water depth, riverbed geometry, flow velocity,
237 ship velocity and position data. Based on this information and by constantly checking the camera's live footage
238 on deck, the camera was lowered or lifted to keep the bed in camera sight and avoid colliding with it. The sufficient
239 camera – riverbed distance depended on the suspended sediment concentration near the bed and the used
240 illumination. The reel was equipped with a register, with its zero adjusted to the water surface. This register was
241 showing the length of cable already released under the water, effectively the rough distance between the water
242 surface and the camera (i.e., the end of the cable). Of course, due to the drag force this distance was not vertical,
243 but this value could be continuously compared to the water depth measured by the ADCP. Differencing these two
244 values, an approximation for the camera – riverbed distance was given all time. The sufficient difference could
245 be established by monitoring the camera footage while lowering the device towards the bed. This value was then
246 to be maintained with smaller corrections during the survey of the given cross-section, always supported by
247 observing the camera recording, and adjusting to environmental changes. The vessel's speed was also adjusted
248 based on the video and slowed down if the video was blurry or the camera got too far away from the bed (see later
249 in Section 3.3). The measurements required three personnel to i) drive the vessel, ii) handle the reel, adjust the
250 equipment position, and monitor the camera footage, iii) monitor the ADCP data, while communicating with the
251 other personnel (see Fig. 3).



252
253
254
255

Figure 3: Left: sketch of the measurement process. The vessel was moving perpendicular to the riverbank along a cross-section (i). A reel was used to lower a camera close to the riverbed (ii). Simultaneously, the bed topography and water depth were measured by an ADCP (iii). Right: Close-up sketch of the underwater instrumentation.

256 The video recordings were made with a GOPRO Hero 7 and a Hero 4 commercial action cameras. Image
257 resolutions were set to 2704x2028 (2.7K) with 60 frame per second (fps) and 1920x1080 (1080p) with 48 fps,
258 respectively. Other parameters were left at their default (see GOPRO 2014; 2018), resulting in slightly different
259 quality of produced images between the two cameras. We found that a 0.2-0.45 m/s vessel speed with 60 fps
260 recording frequency was ideal to retrieve satisfactory images in a range of 0.4-1.6 m camera-bed distances. This
261 meant approximately 15 minutes long measurements per transects. Further attention needed to be paid to the reel
262 and its cable during the crossing when the equipment was on the upstream side of the boat. If the flow velocities
263 are relatively high (compared to the total submerged weight of the underwater equipment), the cable can be pressed
264 against the vessel-body due to the force from the flow itself, causing the reel cable to jump to the side and leave
265 its guide. This results in the equipment falling to the riverbed and the measurement must be stopped to reinstall
266 the cable. For illumination, a diving light with 1500 lumen brightness and 75° beam divergence, and one with
267 1800 lumen and 8° were used. The four lasers for scaling had 450-520 nm (purple and green) wavelength and 1-
268 5 mW nominal power. Power supply was ensured with batteries for all instruments.

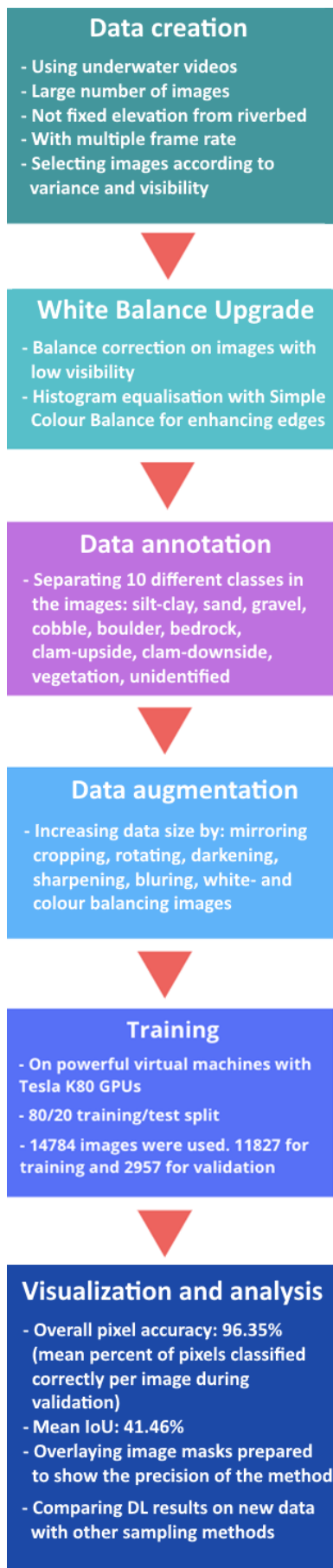
269
270
271
272
273
274

At Site A and Site B, conventional bed material (physical) samplings were also carried out by a grabbing (bucket)
sampler along the analysed transects. At each cross-section 4-5 samples were taken, with one exception where we
had 10. The measured GSDs were used to validate results of the AI algorithm. Separately, a visual evaluation of
the videos was also carried out, where a person divided the transects into subsections based on their dominant
sediment classes, after watching the footages.

275 **2.3 Image analysis: Artificial Intelligence and the wavelet method**

276 In this study, we built on the former experiences of the authors, using Benkó et al., 2020 as a proof-of-concept,
277 where the developed algorithm was applied for analysing drone videos of a dry riverbed. The same architecture
278 was used in this manuscript, which is based on the widely used Google's DeeplabV3+ Mobilnet, in which many
279 novel and state-of-the-art solutions are implemented (e.g., Atrous Spatial Pyramid Pooling; Chen et al., 2018).
280 The model was implemented with Pytorch, exploiting its handy API and backward compatibility. The main goal
281 was to build a deep neural network model which can recognise and categorise (via semantic segmentation; Chen
282 et al., 2018) at least three main sediment size classes, i.e., sand, gravel and cobble, in the images, while being
283 quickly deployable. The benefit of the introduced method compared to conventional imagery methods lies in the
284 potential of automation and increased speed. If the annotation and training is carried out thoroughly, analysing
285 further videos can run effortlessly, while the computation time can be scaled down either vertically (using stronger
286 GPUs) or horizontally (increasing the number of GPUs; if parallel analysis of images is desired). In this study a
287 TESLA K80 24GB GDDR5 348bit GPU, an Intel Skylake Intel® Xeon® Gold 6144 Processor (24.75M Cache,
288 3.50 GHz) CPU with 13GB RAM was used. Also, contrary to other novel image-processing approaches in riverine
289 sediment research (Buscombe, 2013; Detert and Weitbrecht, 2013), the deep convolutional neural network is
290 much less limited by image resolution and mm/pixel ratios, because it does not rely on precise pixel count. This
291 is an important advantage to be exploited here, as we perform non-scaled training and measurements with the AI,
292 i.e., camera-bed distance constantly changed, and size-reference was not used in the images by the AI.

293
294 Fig. 4 presents the flowchart of our DL-based image processing methodology. The first step after capturing the
295 videos was to cut them into frames, during which the videos were exploded into sequential images. Our
296 measurement setup proved to be slightly nose-heavy. Due to this, and the drag force combined, the camera tilted
297 forward during the measurements. As a result, the lower parts of the raw images were sometimes too dark, as the
298 camera was looking over the riverbed, and not at the lit part of the bed. In this manuscript, this problem was
299 handled by simply cutting out the lower 25% of the images as this was the region usually containing the dark,
300 unlit areas. Brightening and sharpening filters were applied on the remaining part of the images to improve their
301 quality. Next, the ones with clearest outlines and best visibility were chosen. This selection process was necessary
302 because this way the delineation process (learning the prominent characteristics of each class) can be executed
303 accurately, without the presence of misleading or confusing images, e.g., blurry or dark pictures where the features
304 are hard to recognise. For training purposes, we chose three videos from different sections each being ~15 minutes
305 long with 60 fps and 48 fps, resulting in 129 600 frames. In fact, such a large dataset was not needed due to the
306 strong similarity of the consecutive frames. The number of images to be annotated and augmented were therefore



decreased to ~2000. We also performed a white balance correction on some of the images to improve visibility, making it even easier to later define the sediment class boundaries. We used an additional algorithm to generate more data, with the so-called Simplest Colour Balance method (Limare et al., 2011). It is a simple, but powerful histogram equalisation algorithm which helps to equalise the roughness in pixel distribution.

These steps were followed by the annotation, where we distinguished ten classes: silt-clay, sand, gravel, cobble, boulder (mainly riprap), bedrock, clam-upside, clam-downside, vegetation, unidentified (e.g., wreckages). Annotation was carried out by a trained personnel, not by the authors, and performed with the help of an open-source software called PixelAnnotationTool (Breheret, 2017), which enables the user to colour mask large parts of an image based on colour change derivatives (i.e., colour masking part of the images which belong to the same class, e.g., purple/red – sand, green – gravel, yellow – cobble, etc.). The masks and outlines were drawn manually, together with the so-called watershed annotation. That is, when a line was drawn, the algorithm checked for similar pixels in the vicinity and automatically annotated them with the same class. The annotation was followed by a data augmentation step where beside mirroring, cropping, rotating the images (to decrease the chance of overfitting), we also convolved them with different filters. These filters added normally distributed noise to the photos to influence the watershed algorithm and applied sharpening, blurring, darkening, and white balance enhancement. Thus, at the data level, we tried to ensure that any changes in water purity, light, and transparency, as well as colour changes, were adequately represented during training. Images were uniformly converted to 960x540 resolution, scaling them down to make them more usable to fit in the GPU's memory. The next step was to convert all the images from RGB (Red-Green-Blue) based colour to grayscale. This is important because colour images have 3-channels, so that they contain a red, a green, and a blue layer, while grayscale images' pixel can only take one value between 0 and 255. With this colour conversion we obtained a threefold increase in computational speed. In total, a dataset of 14,784 human-annotated images was prepared (from the ~2000 images of the 3 training videos). The next step was to separate this dataset into training and validation sets. In this study, 80% of it was used for training the Deep Learning algorithm, while 20% was withheld and reserved for the validation of the training. It was important to mix the images so that the algorithm selects batches in a pseudorandom manner during training, thus preventing the model from being overfitted.

Figure 4: Flowchart of the applied methodology.

347 Finally, after several changes in the hyperparameters (i.e., tuning), the evaluation and visualisation of the training
348 results were performed. Tuning is a general task to do when building Deep Learning Networks, as these
349 hyperparameters determine the structure of the network and the training process itself. Learning rate, for example,
350 describes how fast the network refreshes, updates itself during the training. If this parameter is set too high, the
351 training process finishes quickly, but convergence may not be reached. If it is too low, the process is going to be
352 slow, but it converges. For this reason, nowadays the learning rate decay technique is used, where one starts out
353 with a large learning rate, then slowly reduces it. The technique generally improves optimization and
354 generalization of the Deep Learning Networks (You et al., 2019). In our case, learning rate was initialised to 0.01,
355 with 30000 iteration steps, and the learning rate was reset after every 5000 iterations with a decay of 0.1. Another
356 important parameter was the batch size, which sets the number of samples fed to the network before it updates
357 itself. Theoretical and empirical evidence suggest that learning rate and batch size are highly important for the
358 generalization ability of a network (He et al., 2019). In our study, a batch size of 16 was used (other general values
359 in the literature are 32, 64, 128, 256). We used a cross-entropy loss function.

360
361 As previously mentioned, the training of the DL algorithm was managed without scaling, without the need for
362 equipped lasers. However, we intended to use the laser pointers to provide a spatial scale for the recorded videos,
363 as a secondary validation. As the lasers were not functioning as we originally hoped, we could not use them
364 constantly during the cross-sectional surveys and could not aim for transactional scaling and validation this way.
365 Instead, we diverted to validation in the points of the physical samplings as we could use the lasers in a few,
366 selected points only. We used a textural image-processing method to analyse the video images of these sampling
367 spots. For this, the already mentioned, transferable wavelet-based signal- and image-processing method was
368 chosen. The method enables to calculate the image-based grain size distribution of the selected pictures. The grey-
369 scale intensity is analysed through pixel-rows and -columns of the image and handled as individual signals. Then,
370 instead of Fourier-transform, the less-constrained wavelet-transform is applied to decompose them. Finally,
371 calculating the power spectra and the sizes (from pixel to millimetre, using the scale) of the wavelet components
372 (each wavelet describes an individual grain) produces the grain size distribution for the given image. Beforehand,
373 this method was proved to be the most efficient, non-DL image-processing method for mixed sediments
374 (Buscombe, 2013; 2020) and was already tested for underwater circumstances in an earlier study (Ermilov et al.,
375 2020).

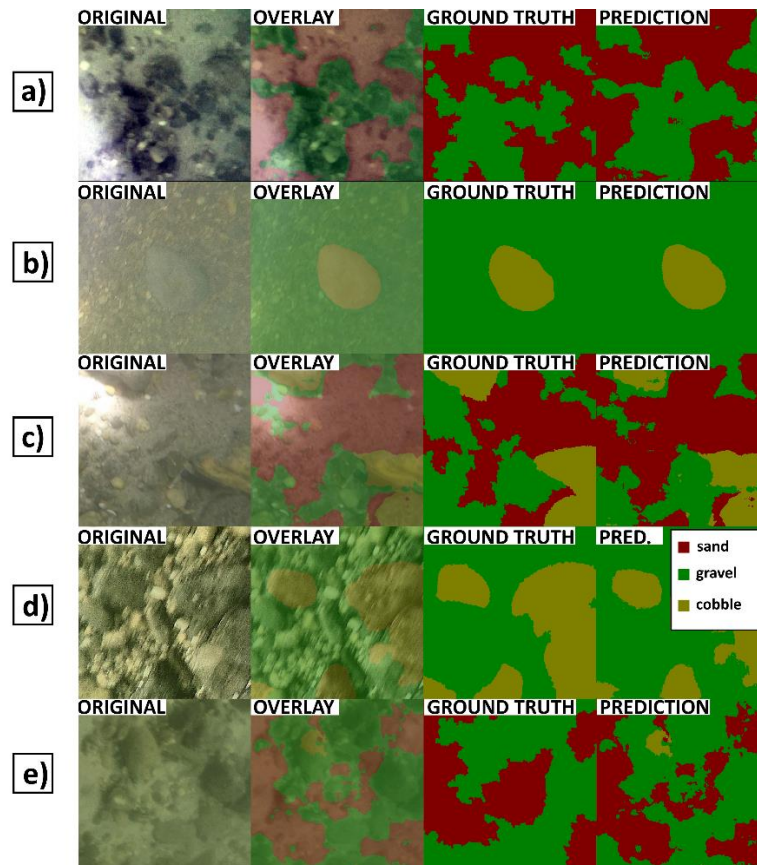
376 **3 Results and discussion**

377 **3.1 Evaluation of the training**

378 To evaluate the training process, the 2957 images of the validation set were analysed by the developed Deep
379 Learning algorithm and the given DL-results were then compared to their human-annotated counterparts. Fig. 5a-
380 d shows results of original images (from the validation set), their ground truth (annotation by the training
381 personnel), as well as the DL prediction (result of the model). The overlays of the original and the predicted
382 images are also shown for better visualization. Calculating the overall pixel accuracy (i.e., the percent of pixels
383 that were correctly classified during validation) returned a satisfactory result with an average 96% match (over
384 the 2957 validation images, each having 960x540 resolution, adding up to a total of 1 532 908 800 pixels as

385 100%). As this parameter in object detection and Deep Learning is not a stand-alone parameter (i.e., it can still be
 386 high even if the model performs poorly), the mean IoU (intersection-over-union or Jaccard index) was also
 387 assessed, indicating the overlap of ground truth area and prediction area, divided by their union (Rahman and
 388 Wang, 2016). This parameter showed a much slighter agreement of 41.46%. Interestingly, there were cases, where
 389 the trained model gave better result than the annotating personnel. While this highlighted the importance of
 390 thorough and precise annotation work, it also showcased that the number of poor annotations was relatively low,
 391 so that the algorithm could still carry out correct learning process and later detections, while not being severely
 392 affected by the mistake of the training personnel. Fig. 5e showcases an example for this: the correct appearance
 393 of cobble (yellow) in the prediction, even though the user (ground truth) did not define it during annotation. As a
 394 matter of fact, these false errors also decrease the IoU evaluation parameter, even though they increase the
 395 performance of the DL algorithm on the long term. Hence, this shows that pure mathematical evaluation may not
 396 describe the model performance entirely. Considering that others also reported similar experience with Deep
 397 Learning (Lu et al., 2018) and the fact that 40% and 50% are generally accepted IoU threshold values (Yang et
 398 al., 2018; Cheng et al., 2018; Padilla et al., 2020), we considered the 41.46% acceptable, while noting that the
 399 annotation and thus the model can further be improved. The general quality of our underwater images may have
 400 also played a role in lowering the IoU result.

401

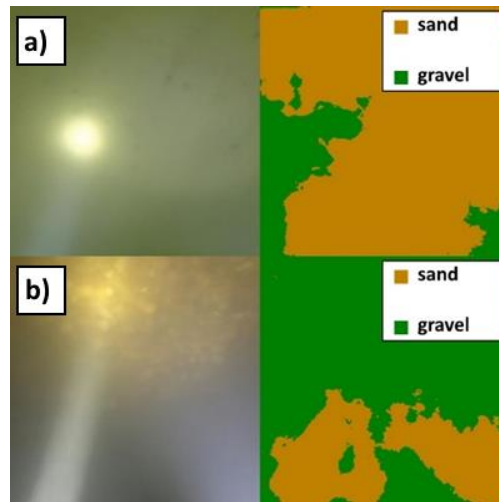


402

403 **Figure 5: a-d) Example comparisons of ground truth (drawn by the annotating personnel, 3rd column) and DL**
 404 **predicted (result of analysing the raw image by the previously trained DL model, 4th column) during the validation**
 405 **process. The 1st column shows raw images, while the 2nd column overlays the result of the DL detection on the raw**
 406 **image for better visual context. e) Example of training personnel mistake during the annotation (i.e., lack of**
 407 **cobble/yellow annotation in ground truth) and how the DL performed better by hinting at the presence of the cobble**
 408 **fraction, leading to a false negative result during validation.**

409
410
411
412
413
414
415
416
417

One of these quality issues for the DL algorithm was associated with the illumination. Using a diving light with small beam divergence proved counterproductive. The high intensity, focused light occasionally caused overexposed zones (white pixels) in the raw bed image, misleading the DL algorithm and resulting in detection of incorrect classes there (Fig. 6a). In darker zones, where the suspended sediment concentration was higher and at the same time, the effect of camera tilting was not completely removed by preprocessing, the focused light sometimes reflected from the suspended sediment itself and resulted in brighter patches in the images (Fig. 6b). This also caused false positive detections.



418
419
420

Figure 6: The effect of strong diving light on the DL algorithm. a) Purely sand covered zone. b) Darker zone with higher SSC. The original images are on the left, while the DL detections can be found on the right.

421

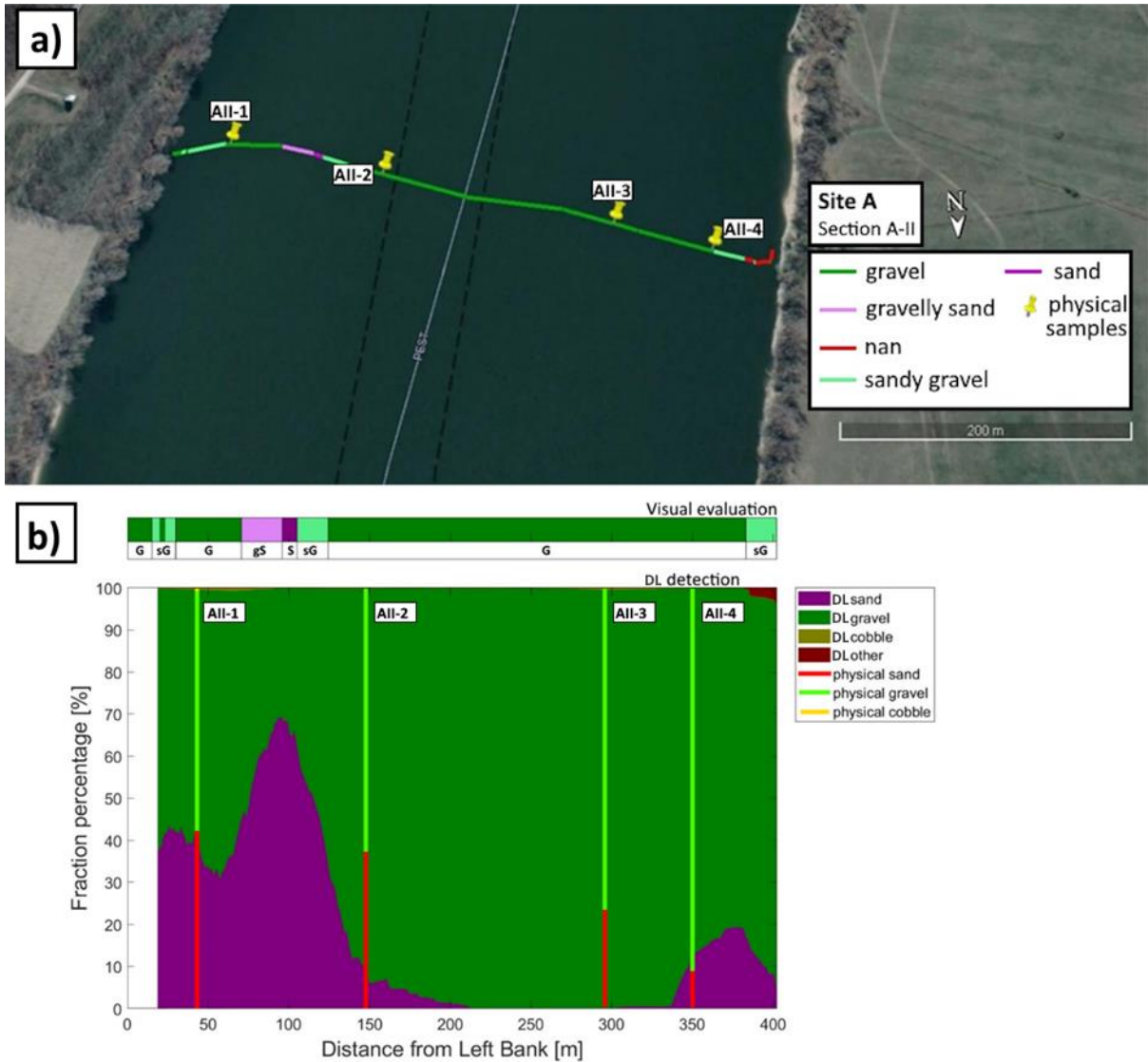
422 3.2 Comparison of methods

423
424
425
426
427
428
429
430
431
432
433
434
435

In each masked image, the occurring percentage of the given class (i.e., the percentage of the pixels belonging to that class/colour mask, compared to the total number of pixels in the image) was calculated and used as the fraction percentage in that given sampling point. These sediment classes reconstructed by the DL algorithm were then compared to three alternative results: i) visual estimation, ii) GSD resulted from conventional grab sampling, iii) wavelet-based image-processing. In the followings, results from two cross-sections will be highlighted, one from Site A, the video used for the training, and one from Site B, being new for the DL. An averaging window of 15 m was applied on each cross-sectional DL result to smoothen and despike the dataset. The interval of physical sample collection in wider rivers can range anywhere between 20-200 m within a cross-section, depending on the river width and the homogeneity of riverbed composition. The averaging window size was chosen to be somewhat lower than our average applied physical sampling intervals in this study, but still in the same order of magnitude. The scope of the present manuscript did not include further sensitivity analysis of the window size. In the followings, the reader is led through the comparison process via the example of two transects, and is given the over-all evaluation of the accuracy of the method.

436 3.2.1 Visual evaluation and physical samples

437 In Fig. 7a, the path of the vessel can be seen in Section A – II, at Site A. The path was coloured based on the visual
438 evaluation of the riverbed images. The different colours represent the dominant sediment type seen at the given
439 point of the bed. The locations of the physical bed material samplings are also shown (see yellow markers). App.
440 Fig. A1 presents the raw (i.e., before moving-average) results of the DL detection of each analysed image along
441 Section A – II. Currently, our approach is sensitive and large spikes, differences can occur in the DL detection
442 between consecutive, slightly displaced video frames. Due to this, and the fact that there is uncertainty in the
443 coordinates of the underwater photos and their corresponding physical samples, it is not recommended to carry
444 out comparisons by selecting certain image and its DL detection. Instead, we applied a moving average-based
445 smoothing for each raw, cross-sectional DL detection, with a window-size corresponding to 15 m at each site.
446 These moving-averages are later used to compare in the sampling points to the physical sampling and the wavelet
447 method. For illustration purposes, we provided the raw DL detections of all the sampling point images in the
448 Appendix, even though their result may not be representative of their corresponding moving-average values. Fig.
449 7b shows the cross-sectional visual classification compared to the DL-detected sediment fractions in percentage
450 after applying moving-average (i.e., the smoothed version of App. Fig. A1). The noises are mostly caused by
451 sudden changes in lighting conditions. It happens either from losing visual on the riverbed momentarily due to
452 sudden topography changes or from increased suspended sediment concentration. The DL result shows
453 satisfactory match with the human evaluation. For example, around 100 m from the left bank, between AII-1 and
454 AII-2 sampling points, the DL algorithm peaks with around 70% sand and 30% gravel correctly. Furthermore, on
455 the two side of this peak a steep transition to gravel and decreasing sand occurs, similarly to the visual observation,
456 marked as sandy gravel and gravelly sand. Mixed sediment zones were also correctly identified by the DL
457 algorithm at both riverbanks.
458



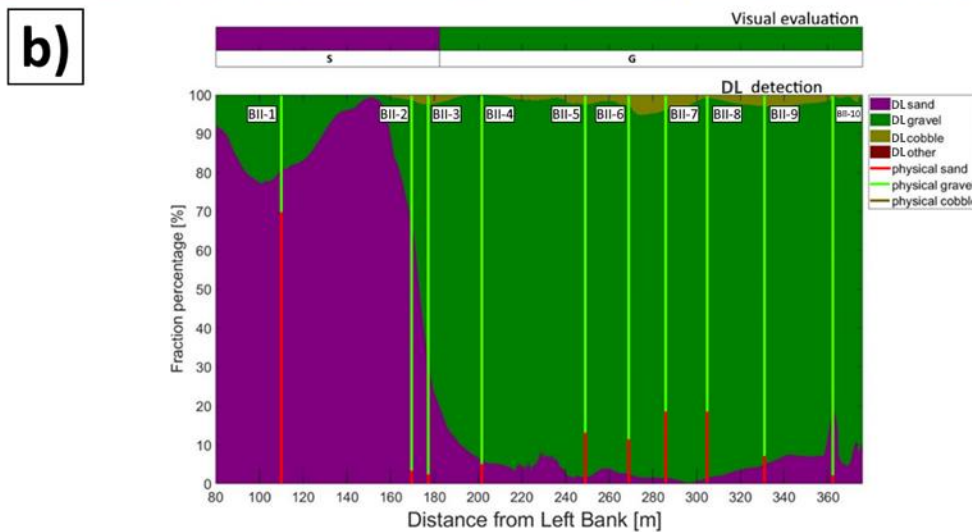
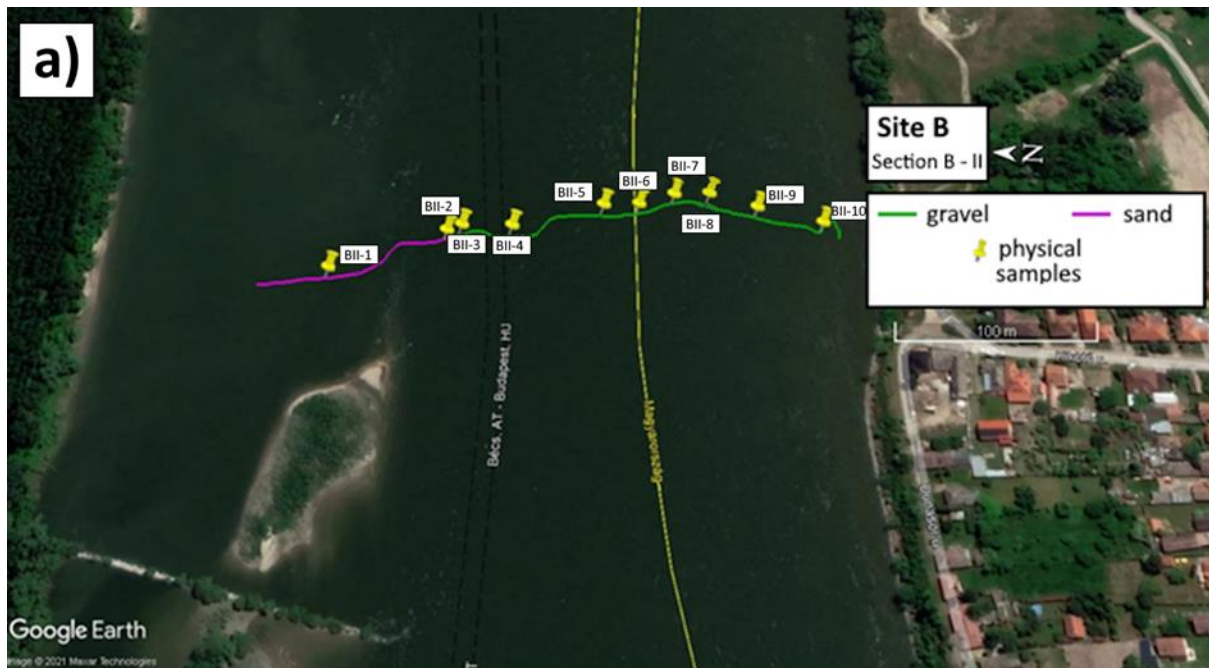
459

460 **Figure 7: a) The path of the vessel and camera in Section A – II, Site A. The polyline is coloured based on the sediment**
 461 **features seen during visual evaluation of the video. Yellow markers are the locations of physical bed material samplings.**
 462 **(Map created with Google Earth Pro). b) The visual evaluation of the dominant sediment features in the video (top)**
 463 **compared to sediment fraction percentage, recognised by the DL algorithm (bottom). DL result after applying moving-**
 464 **averaging. The visual evaluation included four classes: gravel – G, sandy gravel – sG, gravelly sand – gS, sand – S,).**
 465 **The fractions of the physical samples are shown as verticals.**

466

467 At site B (Fig. 8a) the river morphology is more complex compared to Site A as a groyne field is located along
 468 the left bank (see Fig. 2b). As such, the low flow regions between the groynes yield the deposition of fine
 469 sediments, and much coarser bed composition in the narrowed main stream. As it can be seen, the DL algorithm
 470 managed to successfully distinguish these zones: the extension of fine sediments in the deposition zone at the left
 471 bank were adequately estimated and showed a good match with the visual evaluation for the whole cross-section
 472 (see Fig. 8b).

473



474
 475 **Figure 8: a) The path of the vessel and camera in Section–B - II, Site B. The polyline is coloured based on the sediment**
 476 **seen during visual evaluation of the video. Yellow markers are the locations of physical bed material samplings. (Map**
 477 **created with Google Earth Pro). b) Sediment fraction percentages in Section–B - II, recognised by the AI. The visual**
 478 **evaluation included two classes: gravel – G, sand – S). The fractions of the physical samples are shown as verticals.**

479
 480 Results of the other measurements can be found in the Appendix. App. Fig. C2, D2 and E2 show that the trend of
 481 riverbed composition from the visual evaluation is well-captured by the DL algorithm in the other cross-sections
 482 of the study as well.

483
 484 Next, the physically measured and DL-detected relative proportion of sand, gravel and cobble fractions were
 485 compared in each of the 27 sampling points. Firstly, however, outliers had to be identified. In our case, this meant
 486 the separation of sampling points where the differences between the results of the two method were independent
 487 from the efficiency and performance of the DL algorithm. This selection was carried out after analysing the
 488 grainsize distribution curves of the weight-sieved physical samples (App. Fig. F1) and the riverbed images at the
 489 sampling points (App. Fig. A3, B1, C4, D4, E4). Based on our findings, the outliers have been identified and

490 separated into Outlier Type A, and Outlier Type B categories. First category included the sampling points where
 491 the GSD curves showcased bimodal (gap graded) distributions. This type of riverbed sediment distribution is a
 492 typical sign of riverbed armouring (Rákóczi, 1987; Marion & Fraccarollo, 1997), where a coarse surface layer
 493 protects the underlying finer subsurface substrate (see e.g., Wilcock, 2005). While the camera only sees the upper
 494 layer, the bucket sampler can penetrate the surface and gather sample from the subsurface as well. As a result, the
 495 two methods cannot be compared solely on the surface distribution. In App. Fig. A2, supportive images of bed
 496 armouring are provided, taken during our surveys in the Upper section of the Hungarian Danube. Out of the 27
 497 sampling points, 11 was categorised as Outlier Type A. The category of Outlier Type B consisted of points from
 498 the opposite case: where the riverbed image contained fine sediment, but the physical samples did not. In these
 499 cases, a relatively thin layer of fine sediment covered the underlying gravel particles. 2 sampling points were
 500 categorised as Outlier Type B, both of which were near to the borderline between a deposition zone behind a
 501 groyne, and the gravel bedded main channel. In these cases, the bucket sampler probably either stirred up the
 502 deposited fine sediment and washed it down during its lifting or was dragged through purely gravel bedded patch
 503 during sampling, as the surface composition was rapidly changing on this before-mentioned borderline. It is also
 504 worth noting that the physical samples are analysed by weighing the different sediment size classes, resulting in
 505 weight distribution. On the other hand, the imagery methods provide surface distributions, hence having a thin
 506 layer of fine sediments on the top can strongly bias the resulted composition (Bunte and Abt, 2001; Sime and
 507 Ferguson, 2003; Rubin et al., 2007).

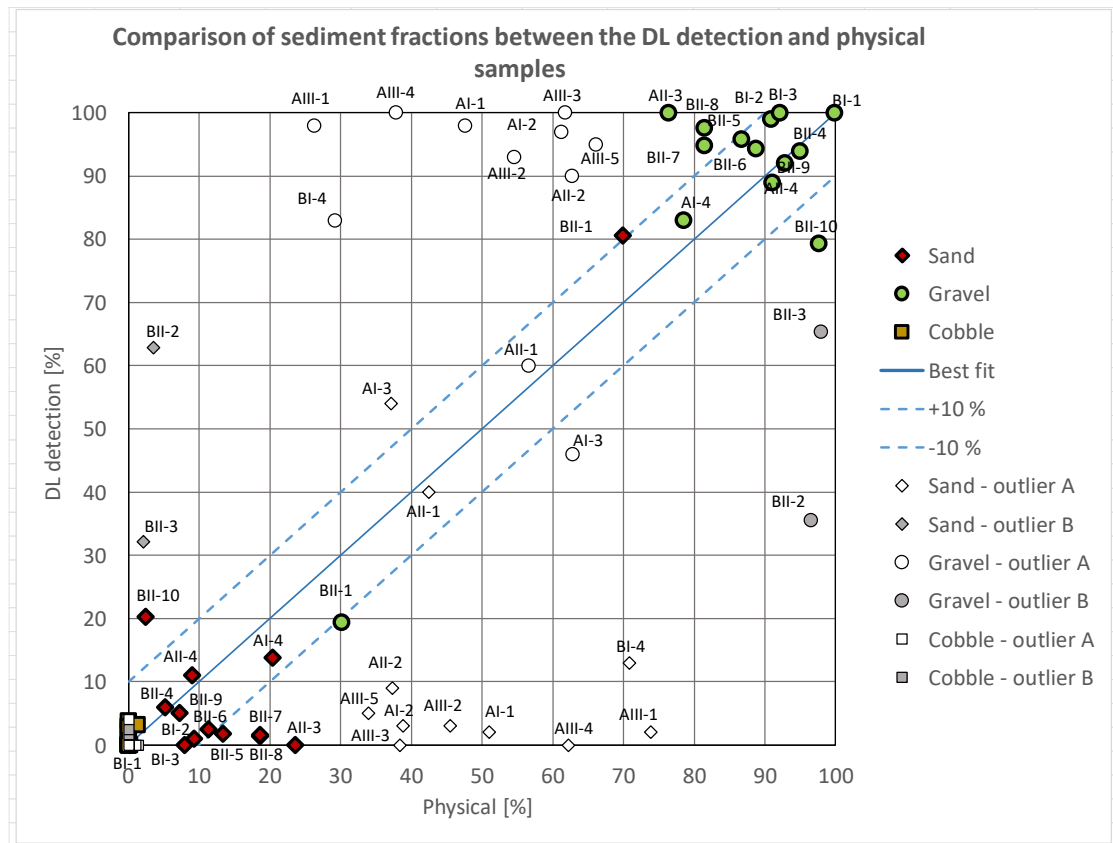
508

	Comparable data	Outlier Type A	Outlier Type B	Σ
No. sampling points	14	11	2	27

509 **Table 2: After evaluating the results of the sieving analyses and riverbed surface images, out of the 27 sampling points,**
 510 **14 were defined as comparable between the applied sampling methods. 11 points were categorised as Outlier Type A,**
 511 **because their GSD curves were bimodal. 2 points were defined as Outlier Type B, since their images showed the**
 512 **presence of fine sediment, while the sieve analyses did not.**

513

514 Overall, the DL-based classification agreed well within the comparable sampling points, with an average error of
 515 4.5% (Fig. 9). It can be seen that even though in outlier points AII-1 and AI-3 the DL algorithm coincidentally
 516 gave good match with the sieving analysis, in the rest of the outlier points the DL- and physical-based results
 517 systematically differ from each other, supporting our outlier selection methodology.



518
 519
 520
 521
 522
 523

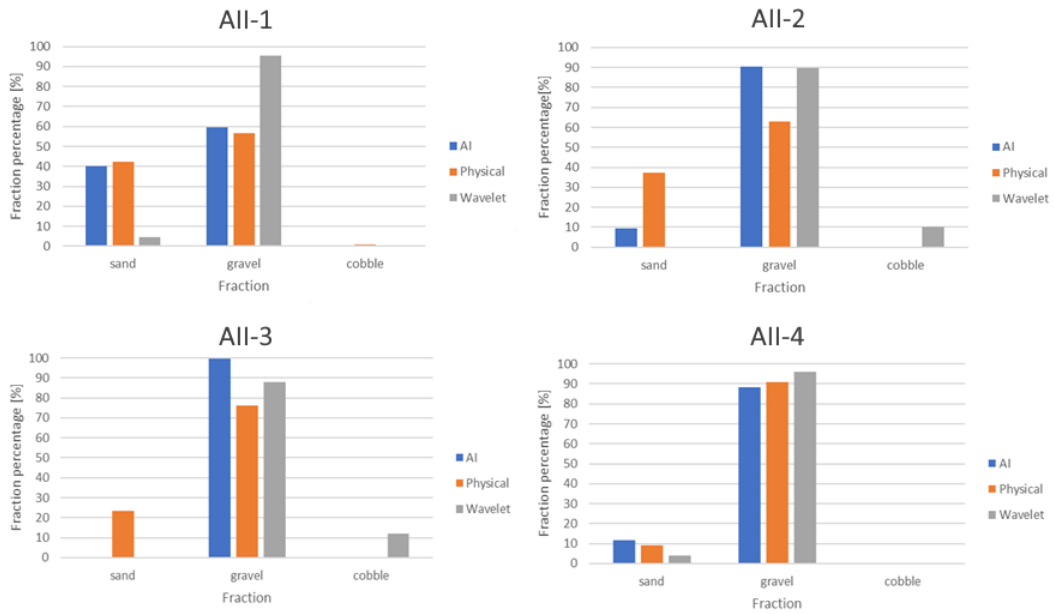
Figure 9: Comparison of relative sediment fractions between the DL detection and physical samples. The three main sediment types (sand-gravel-cobble) are marked with different colour and symbols. The name of the sampling points where the given relative proportion was measured/detected is also written for gravel and sand (cobble was negligible). The proportions of outlier sampling points are marked with white/grey, while the symbol represents the sediment type respectively. The comparable points have their proportions with green (gravel) and red (sand) symbols.

524

525 3.2.1 Wavelet analysis

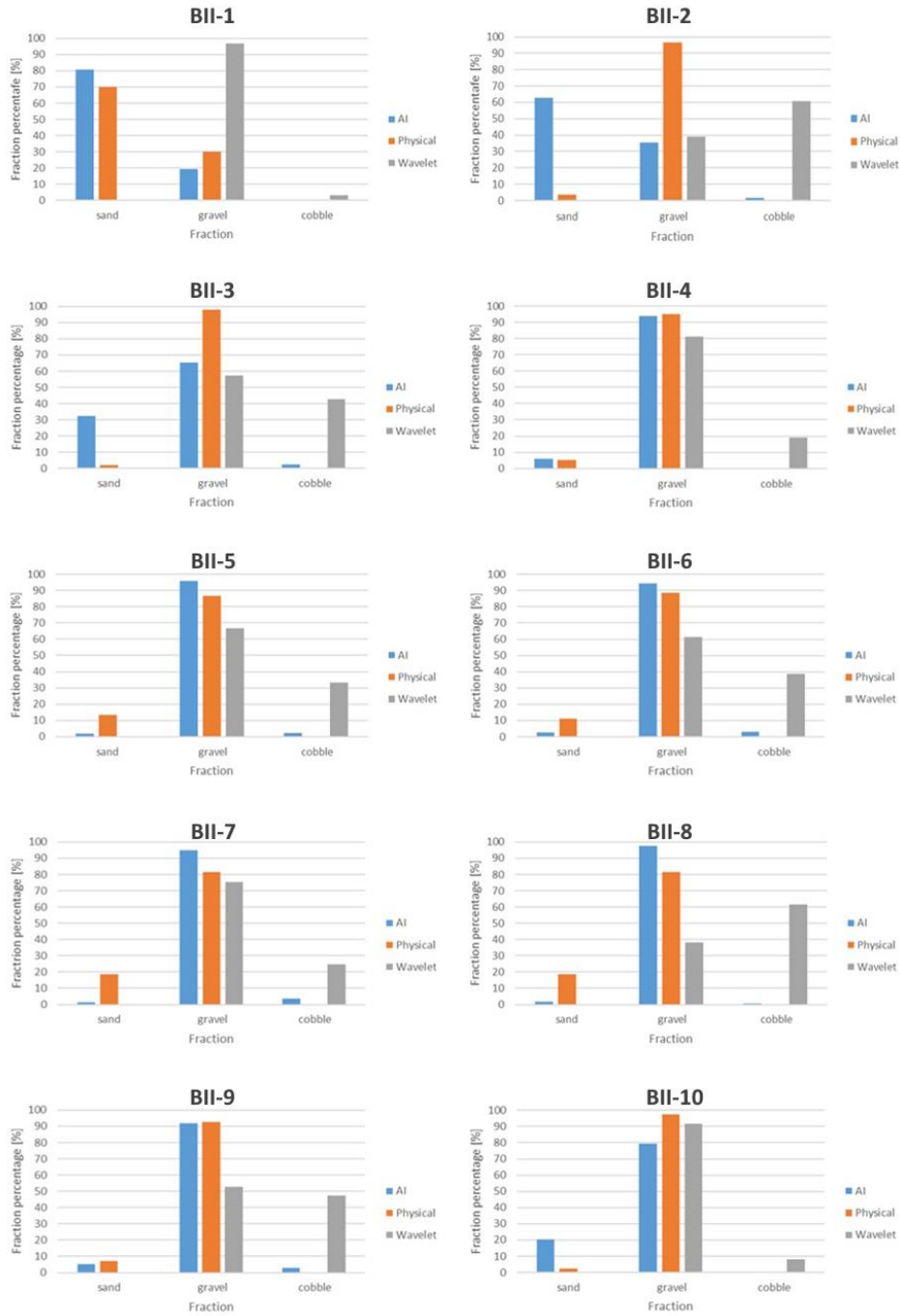
526 As for the wavelet analysis-based imagery technique, an overall slight overestimation of the coarse particles can
 527 be observed, and the sand classes are, in fact, not reconstructed correctly. This finding agrees well with the field
 528 experiences of Ermilov et al. (2020), where the authors indicated the strong sensitivity of the wavelet technique
 529 on the image resolution, and showed that to detect a grain, the diameter must be at least three times larger than
 530 the pixel. In the following, the wavelet-detected relative sediment proportions are compared to the earlier,
 531 corresponding DL-, and physical based ones via bar plots (Fig. 10, 11). For example, the camera was closer to the
 532 riverbed at sampling points AII-1 and AII-4, resulting in a better mm/pixel ratio, hence the wavelet algorithm was
 533 able to detect coarse sand, but finer sand was neglected yielding the lower sand percentages (Fig. 10). In the other
 534 sampling points, where sand was below its resolution, the wavelet method systematically measured the presence
 535 of cobbles instead (Fig. 10), even though the other two methods did not. This trend generally described the
 536 performance of the wavelet method during our study. For visual purposes, an example of the difference in the
 537 capabilities of the two method is given in Fig. 12. While both detected the presence of two major sediment
 538 categories, the wavelet translated the information as gravel and cobble mixture, meanwhile the DL algorithm
 539 recognised the sand coverage and gravel particles.

540



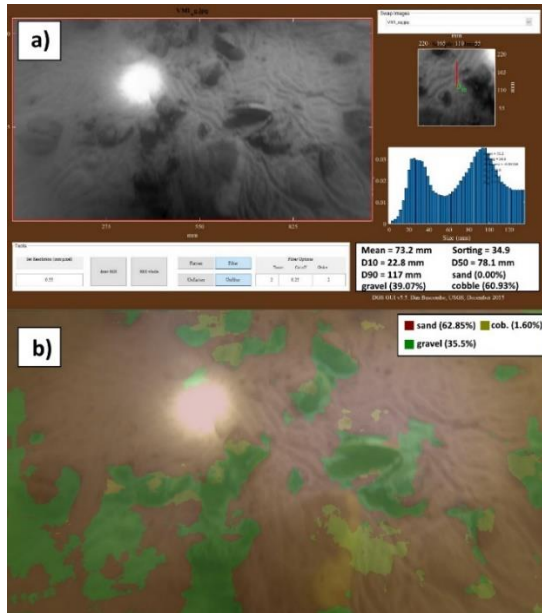
541
 542 **Figure 10: Comparison of relative sediment fraction proportions [%] at the sampling locations from the moving-**
 543 **averaged DL detection, conventional sieving and the wavelet-based image processing method. Section A – II.**

544



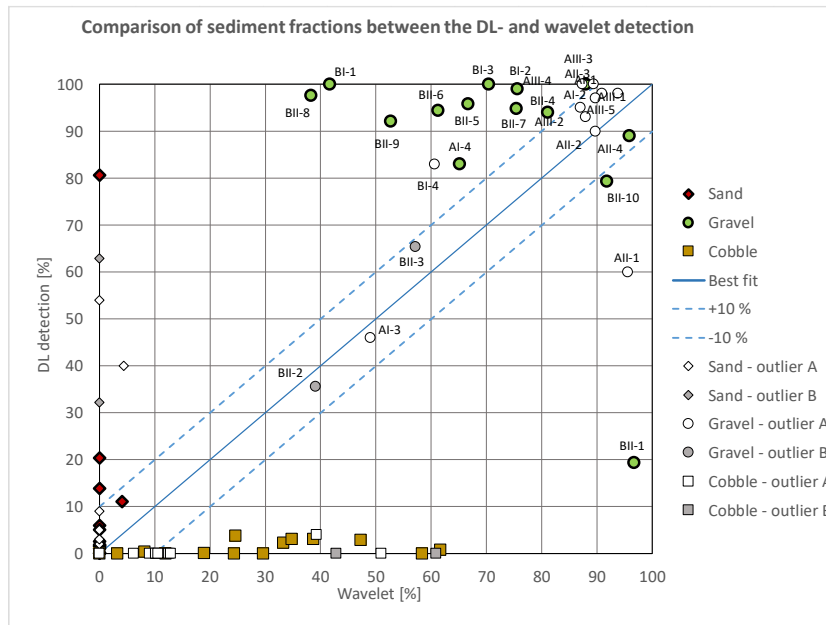
545
546
547

Figure 11: Comparison of relative sediment fraction proportions [%] at the sampling locations from the moving-averaged DL detection, conventional sieving and the wavelet-based image processing method. Section-B - II.



548
 549 *Figure 12: a) Wavelet analysis result of the underwater image in BII-2. b) DL detection result of the same image.*

550
 551 Overall, the comparison between the two image-based method showed greater discrepancies (Fig. 13), due to the
 552 limitations of the wavelet approach, discussed earlier. The same sampling points were labelled as outliers as
 553 earlier. As it can be seen, the wavelet significantly differed in the points where the physical samples and DL-
 554 detections matched (green data points), due to its excessive, false cobble detections. However, it showed good
 555 agreement with the DL in most of the outlier points, supporting that the surface in those points was indeed
 556 composed of solely gravel, and the finer fractions of the physical samples must have come from the subsurface.
 557 Hence, our outlier selection process was well based.



558
 559 **Figure 13: Comparison of sediment fractions between the DL detection and the wavelet approach, for the selected**
 560 **sampling points. The three main sediment types (sand-gravel-cobble) are marked with different colour (red-green-**
 561 **yellow) and symbols (diamond-circle-square) respectively. The name of the sampling points where the given relative**
 562 **proportion was measured/detected is also written for gravel. The proportions of outlier sampling points are marked**
 563 **with white/grey, while the symbol represents the sediment type respectively. The comparable points have their**
 564 **proportions with green (gravel), red (sand) symbols.**

565
566 Based on the results presented in this manuscript, it could be established that the DL algorithm managed to
567 recognise the main features of the riverbed material composition from underwater videos with satisfactory
568 accuracy in the comparable sampling points (compared to the sieving analysis of physical samples) and along
569 cross-sections (based on the visual evaluation). The method showed good potential for mapping heterogenous
570 riverbeds along river cross-sections. Furthermore, the wavelet proved to be a limited comparison tool with the
571 introduced field measurement methodology, as it did not provide it with the sufficient resolution most of the time.
572

573 **3.3 Implementation challenges**

574 The power supply for the entire imaging infrastructure, i.e., for the camera, the diving lights and lasers, was
575 ensured by batteries. However, due to the low temperature at the river bottom, the battery level decreased
576 extremely fast, compared to normal circumstances. Providing the power supply directly from the motorboat
577 engines can overcome this issue. To keep the camera in the adequate height also caused difficulties, since getting
578 too close to the bed can harm the devices, lifting too high, on the other hand, will result in poor image quality.
579 The measured instantaneous ADCP flow depth data was used therefore to keep the bed in camera sight, while
580 maintaining proper boat velocity to avoid blurry images. Choosing a higher recording frequency, however, can be
581 beneficial and alter this limitation, when provided. Lower velocities could not be maintained as the river would
582 have moved the vessel out of the section. An alternative solution can be to move on longitudinal (streamline) paths
583 instead of transects. This would allow for lower vessel speed. This would increase the time of the measurement,
584 which still could be profitable if the images are of higher quality. However, the conventional way for river
585 bathymetry surveys is to move on transversal, cross-sectional paths, due to the river bathymetry having a lower
586 spatial variation along streamlines, compared to the changes that occur in the transversal direction (Benjankar et
587 al., 2015; Kinsman, 2015). As such, it may require carrying out a relatively dense set of longitudinal paths to gain
588 proper information, further increasing the time demand. Thus, for this alternative, higher attention needs to be
589 paid towards choosing these paths and the interpolation method. Another challenge can be the influence of drag
590 force on the measurement setup. In our case, even though the main body itself was a streamlined weight, equipping
591 the other tools on it turned the setup geometry irregular. Additionally, we found that our setup was a bit nose-
592 heavy. On the long term however, this effect could be reduced by building a streamlined container (e.g., 3D-
593 printed body, or a body similar to unmanned underwater vehicles') with slots in it for each device, and also by
594 improving the weight distribution. Furthermore, we hypothesize that by using lasers (as originally planned in this
595 study) during the measurements, the known structure (i.e., the position and distances) of the laser points when the
596 setup is perpendicular to the bed, can help to orthorectify the images. This will decrease the effect of occasional
597 tilting when one wishes to carry out size analysis on the images. In our case, we presented how the wavelet method
598 had inherently bigger issues (i.e., image resolution limit), which could not be caused by the camera tilting since
599 those would be in a significantly lower magnitude of error.

600
601 As for the training of the DL algorithm with the underwater images, the illumination is indeed a more crucial
602 aspect, compared to normal imagery methods. In many cases only the centre areas of the images were clearly
603 visible, whereas the remaining parts were rather dark and shady. Determining the boundaries between distinct
604 sediment classes for these images was challenging even for experienced eyes. This quality issue certainly

605 generated some incorrect annotations. To overcome this issue, manually varying the white balance thus enhancing
606 the visibility of the sediment could improve the training to some extent. It is worth noting that when Deep Learning
607 methods are to be used, most of the problems arise from the data side (Yu et al., 2007), whereas issues related to
608 the applied algorithms and hardware are rare. This is because data is more important from an accuracy perspective
609 than the actual technical infrastructure (Chen et al., 2020). The time demand of image annotation (data
610 preparation) is relatively high, i.e., a trained person could analyse roughly 10 images per hour. On the other hand,
611 as introduced earlier, a great advantage of using DL is the capability of improving the quality of training itself,
612 often yielding better agreement with reality, compared to the manual annotation. Similar results have been
613 reported by Lu et al., (2018). This at the same time proves that with the introduced approach, there is no need for
614 very precise manual training, thus a fast and effective training process can eventually be achieved.

615
616 The validation of the Deep Learning algorithm is far from straightforward. In this study, four approaches were
617 adapted, a mathematical approach, and comparison with three other measurement methods, respectively. The
618 mathematical approach was based on calculating pixel accuracy and the Intersection-over-union parameter, as it
619 is usually done in case of Deep Learning methods to describe their efficiency (e.g., Rahman and Wang, 2016).
620 However, the DL model in some cases overperformed, and provided more accurate results for the sediment
621 composition than the human annotator did. This meant the calculated difference between the annotated validation
622 images and their responding DL-generated result was not solely originated from underperformance of the DL-
623 model, but from human error as well. Consequently, using only the mathematical evaluation in this study could
624 not describe adequately the model performance. Hence, the results were compared to those of three other methods:
625 i) visual evaluation of the image series, ii) a wavelet-based image-processing method (using the method of
626 Buscombe, 2013) and iii) riverbed composition data from physical samples. Considering the features of the
627 applied methods, the first one, i.e., the visual observation, is expected to be the most suitable for the model
628 validation. Indeed, when assessing the bed surface composition by eye, the same patterns are sought, i.e., both
629 methods focus on the uppermost sediment layer. On the other hand, the physical sampling procedure inherently
630 represents subsurface sediment layers, leading to different grain size distributions in many cases. For instance, as
631 shown above, if bed armour develops in the riverbed and the sampler breaks-up this layer, the resulted sample can
632 contain the finer particles from the subsurface layer. On the contrary, in zones where a fine sediment layer is
633 deposited on coarse grains, i.e., a sand layer on the top of a gravel bed, the physical samples represent the coarse
634 material too, moreover, considering that the sieving provides weight distribution this sort of bias will even enhance
635 the proportion of the coarse particles. Attempts were made to involve a third, wavelet-based method for model
636 validation. However, this method failed when finer particles, i.e., sand, characterized the bed. This is an inherent
637 limitation of these type of methods, as discussed earlier, i.e., the pixel size is simply not fine enough to reconstruct
638 the small grain diameters in the range below fine gravel. Lastly, the most comparable sample points were selected
639 to quantify the performance of the DL. Holding the sieved physical samples as ground truth, the DL algorithm
640 showed promising results. The average error (difference) between DL-detected and physically measured relative
641 sediment fraction portion percentages was 4.5%. Furthermore, the DL algorithm successfully detected the trend
642 of changing bed composition along complete river cross-sections.

643

644 As it is known, the ML and DL models can learn unknown relationships in datasets, but unwanted biases as well.
645 With our current dataset, in our opinion, these biases would be the darker tones of visible grain texture and the
646 lack of larger grain sizes. This way our model in its current state is only applicable effectively in the chosen study
647 site, until the dataset is not expanded with additional images from other rivers or regions. However, the purpose
648 of the manuscript was to introduce the methodology itself and its potential in general and not to create a universal
649 algorithm.

650 **3.4 Novelty and future work**

651 The introduced image-based Deep Learning algorithm offers novel features in the field of sedimentation
652 engineering. First, to the authors' knowledge, underwater images of the bed of a large river have not yet been
653 analysed by AI. Second, the herein introduced method enables extensive (and still relatively quick) mapping of
654 the riverbed, in contrast to most of the earlier approaches, where only several points or shorter sections were
655 assessed with imagery methods. Third, the method is much faster compared to conventional samplings or non-
656 DL-based image-processing techniques. The field survey of a 400 m long transect took ~15 minutes, while the
657 DL analysis took 4 minutes (approx. 7 image/s). The speed range of 0.2-0.45 m/s of the measurement vessel and
658 the 15 minutes per transect complies with the operating protocol of general ADCP surveys on rivers (e.g., RD
659 Instruments, 1999; Simpson, 2002; Mueller and Wagner, 2013). Hence, the developed image-based measurement
660 can be carried out together with the conventional boat-mounted ADCP measurements, further highlighting its time
661 efficiency. Indeed, the method is a great alternative approach for assessing riverbed material on-the-go, in
662 underwater circumstances. As an extensive and quick mapping tool, it can support other types of bed material
663 samplings in choosing the sampling locations and their optimal number. Furthermore, it can be used for quickly
664 detecting areas of sedimentation and their extent, as it was shown in Section 3.2. (e.g., Fig. 12b). This way, it may
665 support decisions regarding the maintenance of the channel or the bank-infiltrated drinking water production
666 (detecting colmation and colmated zones). Fourth, a novel approach was used for the imaging and model training.
667 As the camera-bed distance were constantly changing, the mm/pixel ratio also varied. Hence, no scale was defined
668 for the algorithm beforehand. Earlier Deep Learning methods for sediment analysis all applied fixed camera
669 heights and/or provided scaling for the AI. It should be noted that these were airborne measurements, mapping
670 the dry zone of the rivers. In an underwater manner, it is extremely challenging to keep a fixed, constant camera
671 height due to the spatially varying riverbed elevations. Hence, it is of major importance that this manuscript
672 introduces a methodology and a Deep Learning algorithm which neglect the need for scaling. This way, the
673 method is faster and easier to build, but also simpler to use. Of course, as a trade-off, the method, as of now,
674 cannot reconstruct detailed grainsize distributions. Indeed, the purpose was rather to provide a uniquely fast bed
675 material mapping tool, additionally with a much denser spatial resolution than the conventional methods, saving
676 up significant resources.

677
678 Originally, beside the three main sediment grain classes introduced in the manuscript (sand, gravel, cobble), others
679 were also defined during annotation (e.g., bedrock, clams), but due to class imbalance (i.e., dominance of the three
680 sediment classes), these were not adapted successfully. There is a good potential in improving the method through
681 transfer learning (see Zamir et al., 2018) using broader dataset, involving other sediment types. Another possible

682 way to counter imbalance is the use of so-called weighted cross entropy (see Lu et al., 2019) on the current dataset,
683 which will also be investigated in our case.

684

685 Since the introduced method offers a quick way to provide extensive, spatially dense bed material information of
686 its composition, it may be used to boost the training dataset of predictive, ensemble bagging-based Machine
687 Learning techniques (e.g., Ren et al., 2020) and improve their accuracy. Furthermore, the method can support the
688 implementation of other imagery techniques. For instance, using one of the training videos of this study the authors
689 managed to reconstruct the grain-scale 3D model of a riverbed section with the Structure-from-Motion technique
690 (Ermilov et al., 2020), enabling the quantitative estimation of surface roughness. Underwater field cameras can
691 also be used for monitoring and estimating bedload transport rate (Ermilov et al., 2022) by adapting LS-PIV and
692 the Statistical Background Model approach. This latter videography technique may also be used with moving
693 cameras (e.g., Hayman and Ekhlund, 2003), which enables its adaptation into our method by e.g., detecting
694 bedload movement in the cross-section.

695

696 The statistical representativity of the introduced method, as a surface sampling technique, needs to be also
697 addressed in future work. Following and building upon the experience of conventional, surface sampling
698 procedures (e.g., grid sampling; Diplas, 1988) may prove to be beneficial, where they provided the exact number
699 of gravel particles needed to be included (Wolman, 1954) to satisfy the representativity criteria. Then, using edge-
700 and blob-detection would enable to calculate and compare the number of gravel particles in the images to this
701 value. Furthermore, we intend to apply 2 cameras, with overlapping FOVs for increasing the covered area (and
702 the representativity) during surveys. Besides, it would also improve the accuracy of the Structure-from-Motion
703 technique mentioned earlier.

704 **4 Conclusion**

705 A novel, artificial intelligence-based riverbed sediment analysis method has been introduced in this manuscript,
706 which uses underwater images to reconstruct the spatial variation of the characteristic sediment classes. The
707 method was trained and validated with a reasonably high number (~15000) of images, collected in a large river,
708 in the Hungarian section of the Danube. The main novelties of the developed Deep Learning based procedure are
709 the followings: i) underwater images are used, ii) the method enables mapping of the riverbed along the
710 measurement vessel's route with very dense spatial allocation, iii) cost-efficient, iv) works without scaling, i.e.,
711 the distance between the camera and the riverbed can vary. Consequently, in contrast with conventional pointwise
712 bed sediment analysis methods, this technique is robust and capable of providing continuous sediment
713 composition data covering whole river reaches, eventually providing the possibility to set up 2D bed material
714 maps. In this way, river reach scale hydromorphological assessments can be supported, where the composition of
715 bed surface is of interest, e.g., when performing habitat studies, parameterising 2D and 3D computational
716 hydrodynamic and morphodynamic models, or assessing the impact of restoration measures.

717 **Financial support.** The first author acknowledges the support of the ÚNKP-21-3 New National Excellence
718 Programme of the Ministry for Innovation and Technology, and the National Research, Development and
719 Innovation Fund, Hungary.

720 **Code availability.** The code written and used in this manuscript is available here: [https://bmeedu-](https://bmeedu-my.sharepoint.com/:f/g/personal/ermilov_alexander_emk_bme_hu/EjI2neM4AOZGsBkYgKReViEBBzRFRFoYyLlmo6SzTB_qDQ?e=AqqqHI)
721 [my.sharepoint.com/:f/g/personal/ermilov_alexander_emk_bme_hu/EjI2neM4AOZGsBkYgKReViEBBzRFRFo](https://bmeedu-my.sharepoint.com/:f/g/personal/ermilov_alexander_emk_bme_hu/EjI2neM4AOZGsBkYgKReViEBBzRFRFoYyLlmo6SzTB_qDQ?e=AqqqHI)
722 [YyLlmo6SzTB_qDQ?e=AqqqHI](https://bmeedu-my.sharepoint.com/:f/g/personal/ermilov_alexander_emk_bme_hu/EjI2neM4AOZGsBkYgKReViEBBzRFRFoYyLlmo6SzTB_qDQ?e=AqqqHI)

723 **Data availability.** The dataset and results can be accessed using the following link: [https://bmeedu-](https://bmeedu-my.sharepoint.com/:f/g/personal/ermilov_alexander_emk_bme_hu/EhoGx64sP1tFnj8Z1OdMZAsBZWd5gDYzPyodSUDdWFjeiw?e=hKIXjq)
724 [my.sharepoint.com/:f/g/personal/ermilov_alexander_emk_bme_hu/EhoGx64sP1tFnj8Z1OdMZAsBZWd5gDY](https://bmeedu-my.sharepoint.com/:f/g/personal/ermilov_alexander_emk_bme_hu/EhoGx64sP1tFnj8Z1OdMZAsBZWd5gDYzPyodSUDdWFjeiw?e=hKIXjq)
725 [zPyodSUDdWFjeiw?e=hKIXjq](https://bmeedu-my.sharepoint.com/:f/g/personal/ermilov_alexander_emk_bme_hu/EhoGx64sP1tFnj8Z1OdMZAsBZWd5gDYzPyodSUDdWFjeiw?e=hKIXjq)

726 **Author contributions.** GB developed the code and carried out the training process. AAE carried out the
727 fieldwork, evaluated the results, did the laboratory analysis, and collaborated with GB in improving the images.
728 SB oversaw and directed the project, while managing the financial- and equipment background.

729 **Competing interest.** The contact author has declared that none of the authors has any competing interest.

730 **Acknowledgements.** The authors would like to thank our students Dávid Koós, Gergely Tikász, Schrott Márton
731 and our technicians István Galgóczy, István Pozsgai, Károly Tóth and András ReháK for fieldwork support.

732 **References**

733 Adams, J.: Gravel Size Analysis from Photographs. J. Hydraul. Div., 1979, 105, 1247–1255.
734 doi/10.1061/JYCEAJ.0005283, 1979.

735
736 Anglin, D. R., Haeseker, S. L., Skalicky, J. J., Schaller, H., Tiffan, K. F., Hatten, J. R., et al.: Effects of Hydropower
737 Operations on Spawning Habitat, Rearing Habitat, and Standing/Entrapment Mortality of Fall Chinook Salmon
738 in the Hanford Reach of the Columbia River. US Fish and Wildlife Service, final Report. Available at:
739 <https://pubs.er.usgs.gov/publication/70179516>, 2006.

740
741 Baranya, S., Fleit, G., Józsa, J., Szalóky, Z., Tóth, B., Czeglédi, I. and Erős, T.: Habitat mapping of riverine fish
742 by means of hydromorphological tools. Ecohydrology, Volume 11, Issue 7 e2009. Available at:
743 <https://doi.org/10.1002/eco.2009>, 2018.

744
745 Barnard, P., Rubin, D., Harney, J. and Mustain, N.: Field test comparison of an autocorrelation technique for
746 determining grain size using a digital beachball camera versus traditional methods. Sedimentary Geology, 201(1–
747 2): 180–195., 2007.

748
749 Benjankar, R., Tonina, D., Mckean, J.: One-dimensional and two-dimensional hydrodynamic modelling derived
750 flow properties: Impacts on aquatic habitat quality predictions. Earth Surf. Process. Landf. 2015, 40, 340–356.

751
752 Benkő, G., Baranya, S., Török, T. G., and Molnár, B.: Folyami mederanyag szemösszetételének vizsgálata Mély
753 Tanulás eljárással drónfelvételek alapján (in English: Analysis of composition of riverbed material with Deep
754 Learning based on drone video footages). Hidrológiai Közlöny, 100, 61–69., 2020. Manuscript
755 Breheret, A.: Pixel Annotation Tool. Av. at: <https://github.com/abreheret/PixelAnnotationTool>, 2017.

756
757 Bunte, K. and Abt, S. R.: Sampling Surface and Subsurface Particle-Size Distributions in Wadable Gravel- and
758 Cobble-Bed Streams for Analyses in Sediment Transport, Hydraulics, and Streambed Monitoring; General
759 Technical Report (GTR), U.S. Department of Agriculture, Forest Service, Rocky Mountain Research Station: Fort
760 Collins, CO, USA, 2001.

761
762
763 Buscombe, D. and Masselink, G.: Grain size information from the statistical properties of digital images of
764 sediment. Sedimentology, 56, 421–438. doi/10.1111/j.1365-3091.2008.00977.x, 2008.

765

766 Buscombe, D.: Transferable wavelet method for grain-size distribution from images of sediment surfaces and thin
767 sections, and other natural granular patterns. *Sedimentology*, 60 1709–1732., 2013.
768

769 Buscombe, D., Grams, P. and Kaplinski, M.: Characterizing riverbed sediment using high-frequency acoustics: 1.
770 Spectral properties of scattering. *Journal of Geophysical Research: Earth Surface*, doi: 10.1002/2014JF003189,
771 119:12, (2674-2691), 2014a.
772

773 Buscombe, D., Grams, P. and Kaplinski, M.: Characterizing riverbed sediment using high-frequency acoustics: 2.
774 Scattering signatures of Colorado Riverbed sediment in Marble and Grand Canyons. *Journal of Geophysical
775 Research: Earth Surface*, doi/full/10.1002/2014JF003191, 119:12, (2674-2691), 2014b.
776

777 Buscombe, D. and Ritchie, A. C.: Landscape Classification with Deep Neural Networks. *Geosciences*, 8, 244.
778 Available at: <https://doi.org/10.3390/geosciences8070244> , 2018.
779

780 Buscombe, D.: SediNet: a configurable deep learning model for mixed qualitative and quantitative optical
781 granulometry optical granulometry. *Earth Surface Processes and Landforms*, 45, 638-651. DOI:
782 10.1002/esp.4760, 2020.
783

784

785 Chandler, J., Lane, S. N. and Ashmore, P.: Measuring river-bed and flume morphology and parameterising bed
786 roughness with a KODAK DCS460 digital camera. *International Archives of Photogrammetry and Remote
787 Sensing*, Vol. XXXIII, Part B7., 2000.
788

789 Chen, C., Zhang, P., Zhang, H., Dai, J., Yi, Y., Zhang, H. and Zhang, Y.: Deep Learning on Computational-
790 Resource-Limited Platforms: A Survey. Volume 2020, Article ID 8454327. Available at:
791 <https://doi.org/10.1155/2020/8454327>, 2020.
792

793 Chen, L., Zhu, Y., Isola, P., Papandreou, G., Schroff, F. and Adam, H.: Encoder-Decoder with Atrous Separable
794 Convolution for Semantic Image Segmentation. *Proceedings of the European conference on computer vision
795 (ECCV)* (pp. 801-818). <https://arxiv.org/abs/1802.02611>, 2018.
796

797 Cheng, D., Li, X., Li, W. H., Lu, C., Li, F., Zhao, H. and Zheng, W. S.: Large-Scale Visible Watermark Detection
798 and Removal with Deep Convolutional Networks. In book: *Pattern Recognition and Computer Vision. First
799 Chinese Conference, PRCV, Guangzhou, China, Proceedings, Part III*. DOI: 10.1007/978-3-030-03338-5_3,
800 2018.
801

802 Cheng, Z., and Liu, H.: Digital grain-size analysis based on autocorrelation algorithm. *Sedimentary Geology*, 327,
803 21-31. Available at: <https://doi.org/10.1016/j.sedgeo.2015.07.008>, 2015.
804

805 Chezar, H. and Rubin, D. M.: Underwater Microscope System. United States Patent Office, The United States of
806 America as represented by the Secretary of the Interior, US Patent No. 6,680,795 B2., 2004.
807

808 Church, M. A., McLean, D. G., and Wolcott, J. F.: Sediments transport in Gravel Bed Rivers. Chap.: *Riverbed
809 Gravels: Sampling and Analysis*. John Wiley and Sons, New York, 43–88, 1987.
810

811 Cui, G., Su, X., Liu, Y., & Zheng, S.: Effect of riverbed sediment flushing and clogging on river-water infiltration
812 rate: a case study in the Second Songhua River, Northeast China. *Hydrogeology Journal*, 29(2), 551–565.
813 <https://doi.org/10.1007/s10040-020-02218-7>, 2021.
814

815 Delong, M. D. and Brusven, M. A.: Classification and spatial mapping of riparian habitat with applications toward
816 management of streams impacted by nonpoint source pollution. *Environmental Management*, 15:565-571. DOI:
817 10.1007/BF02394745, 1991.
818

819 Detert, M. and Weitbrecht, V.: User guide to gravelometric image analysis by BASEGRAIN. In *Advances in
820 Science and Research*; Fukuoka, S., Nakagawa, H., Sumi, T., Zhang, H., Eds.; Taylor and Francis Group: London,
821 UK, 2013; pp. 1789–1795. ISBN 978-1-138-00062-9., 2013.
822

823 Diplas, P.: Sampling Techniques for Gravel Sized Sediments. *Journal of Hydraulic Engineering*. DOI:
824 10.1061/(ASCE)0733-9429(1988)114:5(484), 1988.
825

826 Ermilov, A.A., Baranya, S. and Török, G.T.: Image-Based Bed Material Mapping of a Large River. *Water*, 12,
827 916. Available at: <https://doi.org/10.3390/w12030916>, 2020.
828

829 Ermilov, A. A., Fleit, G., Conevski, S., Guerrero, M., Baranya, S., & Rütther, N.: Bedload transport analysis using
830 image processing techniques. *ACTA GEOPHYSICA*, 1895-6572 1895-7455. [http://doi.org/10.1007/s11600-022-](http://doi.org/10.1007/s11600-022-00791-x)
831 00791-x, 2022.
832

833 Fehr, R.: Einfache Bestimmung der Korngrößenverteilung von Geschiebematerial mit Hilfe der
834 Linienzahlanalyse (In English: Simple detection of grain size distribution of sediment material using line-count
835 analysis). *Schweizer Ing. und Archit.*, 105, 1104–1109., 1987.
836

837 Ferdowsi, B., Ortiz, C. P., Houssais, M., & Jerolmack, D. J. (2017). Riverbed armouring as a granular segregation
838 phenomenon. *Nature Communications* 2017 8:1, 8(1), 1–10. <https://doi.org/10.1038/s41467-017-01681-3>
839

840 Fetzer, J., Holzner, M., Plötze, M. and Furrer, G.: Clogging of an Alpine streambed by silt-sized particles –
841 Insights from laboratory and field experiments. *Water Research*, Volume 126, Pages 60-69.
842 <https://doi.org/10.1016/j.watres.2017.09.015>, 2017.
843

844 Geist, D. R., Jones, J., Murray, C. J. and Dauble, D. D.: Suitability criteria analyzed at the spatial scale of redd
845 clusters improved estimates of fall chinook salmon (*Oncorhynchus tshawytscha*) spawning habitat use in the
846 Hanford Reach, Columbia River. *Canadian Journal of Fisheries and Aquatic Sciences*, 57: 1636-1646., 2000.
847

848 Gilcher, M. and Udelhoven, T.: Field Geometry and the Spatial and Temporal Generalization of Crop
849 Classification Algorithms—A Randomized Approach to Compare Pixel Based and Convolution Based Methods.
850 *Remote Sens.*, 13, 775., 2021.
851

852 GOPRO Hero 4 Silver: User Manual. Available at: [https://gopro.com/content/dam/help/hero4-](https://gopro.com/content/dam/help/hero4-silver/manuals/UM_H4Silver_ENG_REVA_WEB.pdf)
853 [silver/manuals/UM_H4Silver_ENG_REVA_WEB.pdf](https://gopro.com/content/dam/help/hero4-silver/manuals/UM_H4Silver_ENG_REVA_WEB.pdf), 2014.
854

855 GOPRO Hero 7 Black: User Manual. Available at: [https://gopro.com/content/dam/help/hero7-](https://gopro.com/content/dam/help/hero7-black/manuals/HERO7Black_UM_ENG_REVA.pdf)
856 [black/manuals/HERO7Black_UM_ENG_REVA.pdf](https://gopro.com/content/dam/help/hero7-black/manuals/HERO7Black_UM_ENG_REVA.pdf), 2018.
857

858 Graham, D. J., Reid, I. and Rice, S. P.: Automated sizing of coarse-grained sediments: image-processing
859 procedures. *Mathematical Geology*, 37, 1–28. <https://doi.org/10.1007/s11004-005-8745-x>, 2005.
860

861 Graham, D. J. Rollet, A.J., Piégay, H. and Rice, S. P.: Maximizing the accuracy of image-based surface sediment
862 sampling techniques. *Water Resour. Res.*, 46, W02508. [https://doi.org/](https://doi.org/10.1029/2008WR006940)
863 [10.1029/2008WR006940](https://doi.org/10.1029/2008WR006940), 2010.
864

865 Grams, P. E., Topping, D. J., Schmidt, J. C., Hazel, J. E. and Kaplinski, M.: Linking morphodynamic response
866 with sediment mass balance on the Colorado River in Marble Canyon: Issues of scale, geomorphic setting, and
867 sampling design, *J. Geophys. Res. Earth Surf.*, 118, 361–381, doi:10.1002/jgrf.20050., 2013.
868

869 Guerit, L., Barrier, L., Liu, Y., Narteau, C., Lajeunesse, E., Gayer, E., Métivier, F.: Uniform grain-size distribution
870 in the active layer of a shallow, gravel-bedded, braided river (the Urumqi River, China) and implications for paleo-
871 hydrology. *Earth Surface Dynamics*. 6. 1011-1021. DOI: 10.5194/esurf-6-1011-2018., 2018.
872

873 Guerrero, M., Rütther, N., Szupiany, R., Haun, S., Baranya, S. and Latosinski, F.: The Acoustic Properties of
874 Suspended Sediment in Large Rivers: Consequences on ADCP Methods Applicability. *Water*, 8, 13;
875 doi:10.3390/w8010013, 2016.
876

877 Haddadchi, A., Booker, D.J. and Measures, R.J.: Predicting riverbed substrate cover proportions across New
878 Zealand. *Catena*, Volume 163, pp. 130-146. Available at: <https://doi.org/10.1016/j.catena.2017.12.014>, 2018.
879

880 Hayman, E., Eklundh, J.: Statistical Background Subtraction for a Mobile Observer. *Proceedings of the Ninth*
881 *IEEE International Conference on Computer Vision (ICCV 2003) 2-Volume Set 0–7695–1950–4/03*, 2003.
882

883 He, F., Liu, T., Tao, D.: Control batch size and learning rate to generalize well: theoretical and empirical evidence.
884 *Neural Information Processing Systems*, 2019.
885

886 Ibbeken, H., and Schleyer, R.: Photo-sieving: A method for grain-size analysis of coarse-grained, unconsolidated
887 bedding surfaces. *Earth Surf. Process. Landforms*, 11, 59–77. Available at:
888 <https://doi.org/10.1002/esp.3290110108>, 1986.

889

890 Igethinathane, C., Melin, S., Sokhansanj, S., Bi, X., Lim, C. J., Pordesimo, L. O. and Columbus, E. P.: Machine
891 vision based particle size and size distribution determination of airborne dust particles of wood and bark pellets.
892 *Powder Technol.*, 196, 202–212. Available at: <https://doi.org/10.1016/j.powtec.2009.07.024>, 2009.

893

894 Kellerhals, R. and Bray, D. I.: Sampling Procedures for Coarse Fluvial Sediments. *J. Hydraul. Div.*, 97, 1165–
895 1180., 1971.

896

897 Kim, H., Han, J. and Han, T. Y.: Machine vision-driven automatic recognition of particle size and morphology in
898 SEM images. *Nanoscale*, 12, 19461–19469. Available at: <https://doi.org/10.1039/D0NR04140H>, 2020.

899

900 Kinsman, N.: Single-Beam Bathymetry Data Collected in Shallow-Water Areas near Gambell, Golovin, Hooper
901 Bay, Savoonga, Shishmaref, and Wales, Alaska 2012–2013; Department of Natural Resources. Division of
902 Geological & Geophysical Surveys: Fairbanks, AK, USA, 2015.

903

904 Le, Q. V.: Building high-level features using large scale unsupervised learning. In *Proceedings of the 2013 IEEE*
905 *International Conference on Acoustics, Speech and Signal Processing*, Vancouver, BC, Canada, pp. 8595–8598.,
906 2013.

907

908 Leopold, L. B.: An Improved Method for Size Distribution of Stream Bed Gravel. *Water Resour. Res.*, 6, 1357–
909 1366. <https://doi.org/10.1029/WR006i005p01357>, 1970.

910

911 Limare, A., Tal, M., Reitz, M. D., Lajeunesse, E., and Métivier, F.: Optical method for measuring bed topography
912 and flow depth in an experimental flume. *Solid Earth*, 2, 143–154, <https://doi.org/10.5194/se-2-143-2011>., 2011.

913

914 Lowe, D. G.: Distinctive Image Features from Scale-Invariant Keypoints. *International Journal of Computer*
915 *Vision*, 60, pages 91–110, 2004.

916

917 Lu, S., Gao, F., Piao, Ch. and Ma, Y.: Dynamic Weighted Cross Entropy for Semantic Segmentation with
918 Extremely Imbalanced Data. 2019 International Conference on Artificial Intelligence and Advanced
919 Manufacturing (AIAM). doi: 10.1109/AIAM48774.2019.00053, 2019.

920

921 Mueller D. S., Wagner, Ch. R.: Measuring Discharge with Acoustic Doppler Current Profilers from a Moving
922 Boat. USGS, Chapter 22 of Book 3, Section A. <https://pubs.usgs.gov/tm/3a22/>, 2009.

923

924 Muñoz-Mas, R., Sánchez-Hernández, J., McClain, M. E., Tamatamah, R., Mukama, S. C., & Martínez-Capel, F.:
925 Investigating the influence of habitat structure and hydraulics on tropical macroinvertebrate communities.
926 *Ecohydrology and Hydrobiology*, 19(3), 339–350. <https://doi.org/10.1016/j.ecohyd.2018.07.005>, 2019.

927

928 Mueller D. S., Wagner, Ch. R.: Measuring discharge with acoustic Doppler current profilers from a moving boat,
929 version 2.0. [https://www.researchgate.net/publication/284587353_Measuring_discharge_with_acoustic_-_](https://www.researchgate.net/publication/284587353_Measuring_discharge_with_acoustic_-_Doppler_current_profilers_from_a_moving_boat)
930 [Doppler current profilers from a moving boat](https://www.researchgate.net/publication/284587353_Measuring_discharge_with_acoustic_-_Doppler_current_profilers_from_a_moving_boat), 2013.

931

932 Muste, M., Baranya, S., Tsubaki, R., Kim, D., Ho, H., Tsai, H. and Law, D.: Acoustic mapping velocimetry. *Water*
933 *Resour. Res.*, 52, 4132–4150, doi:10.1002/2015WR018354., 2016.

934

935 Obodovskyi, O., Habel, M., Szatten, D., Rozlach, Z., Babiński, Z., Maerker, M.: Assessment of the Dnieper
936 Alluvial Riverbed Stability Affected by Intervention Discharge Downstream of Kaniv Dam. *Water*, 12(4):1104.
937 <https://doi.org/10.3390/w12041104>, 2020.

938

939 Padilla, R., Netto, S. M. and da Silva, E. A. B.: A Survey on Performance Metrics for Object-Detection
940 Algorithms. Conference: 2020 International Conference on Systems, Signals and Image Processing (IWSSIP).
941 DOI: 10.1109/IWSSIP48289.2020, 2020.

942

943 Perez, L. and Wang, J.: The Effectiveness of Data Augmentation in Image Classification using Deep Learning.
944 arXiv preprint arXiv:1712.04621. Av. at: <https://arxiv.org/abs/1712.04621>., 2017.

945

946 Purinton, B. and Bookhagen, B.: Introducing PebbleCounts: A grain-sizing tool for photo surveys of dynamic
947 gravel-bed rivers. *Earth Surf. Dyn.*, 7, 859–877. <https://doi.org/10.5194/esurf-7-859-2019>, 2019.

948

949 Rákóczi, L.: Selective erosion of noncohesive bed materials. *Geografiska Annaler. Series A, Physical Geography*,
950 Vol. 69, No. 1, pp. 29-35. <https://doi.org/10.2307/521364>, 1987.

951

952 Rákóczi, L.: Identification of river channel areas inclined for colmation, based on the analysis of bed material.
953 *Vízügyi Közlemények*, LXXIX., chapter 3., 1997.

954

955 Rahman, M. A. and Wang, Y.: Optimizing Intersection-Over-Union in Deep Neural Networks for Image
956 Segmentation. In: Bebis G. et al. (eds) *Advances in Visual Computing. ISVC 2016. Lecture Notes in Computer
957 Science*, vol 10072. Springer, Cham. https://doi.org/10.1007/978-3-319-50835-1_22, 2016.

958

959 RD Instruments – Acoustic Doppler Current Profilers – Application Note: https://www.commtec.com/library/Technical_Manuscripts/RDI/FSA-004%20Model.pdf, 1999.

960

961

962 Rice, S. and Church, M.: Grain size along two gravel-bed rivers: Statistical variation, spatial pattern and
963 sedimentary links. *Earth Surf. Process. Landf.*, 23, 345–363., 1998.

964

965 Ren, H., Hou, Z., Duan, Z., Song, X., Perkins, W.A., Richmond, M. C., Arntzen, E. V. and Scheibe, T. D.: Spatial
966 Mapping of Riverbed Grain-Size Distribution Using Machine Learning. *Front. Water*, 2:551627. doi:
967 10.3389/frwa.2020.551627, 2020.

968

969 Rozniak, A., Schindler, K., Wegner, J. D. and Lang, N.: Drone images and Deep Learning for river monitoring in
970 Switzerland. Semester project. Institute of Geodesy and Photogrammetry, Project, Swiss Federal Institute of
971 Technology (ETH) Zurich, 2019.

972

973 Rubin, D. M.: A simple autocorrelation algorithm for determining grain-size from digital images of sediment. *J.*
974 *Sed. Res.*, 74, 160–165., 2004.

975

976 Rubin, D. M., Chezar, H., Harney, J. N., Topping, D. J., Melis, T. S., Sherwood, C. R.: Underwater microscope
977 for measuring spatial and temporal changes in bed-sediment grain size. *Sedimentary Geology*, Volume 202, Issue
978 3, Pages 402-408, <https://doi.org/10.1016/j.sedgeo.2007.03.020>, 2007.

979

980 Scheder, C., Lerchegger, B., Flödl, P., Csar, D., Gumpinger, C. and Hauer, C.: Riverbed stability versus clogged
981 interstitial: Depth-dependent accumulation of substances in freshwater pearl mussel (*Margaritifera margaritifera*
982 L.) habitats in Austrian streams as a function of hydromorphological parameters. *Limnologica*, Volume 50,
983 January 2015, Pages 29-39. <https://doi.org/10.1016/j.limno.2014.08.003>, 2015.

984

985 Shields, F. D., Jr. and Rigby, J. R.: River habitat quality from river velocities measured using acoustic Doppler
986 current profiler. *Environ. Manage.*; 36(4):565-75. doi: 10.1007/s00267-004-0292-6., 2005.

987

988 Shields, F. D. Jr.: Aquatic Habitat Bottom Classification Using ADCP. *Journal of Hydraulic Engineering*, Vol.
989 136, Issue 5, 2010.

990

991 Sime, L. C. and Ferguson, R. I.: Information on grain-sizes in gravel bed rivers by automated image analysis. *J.*
992 *Sed. Res.*, 73, 630–636., 2003.

993

994 Simpson, M. R.: Discharge Measurements Using a Broad-Band Acoustic Doppler Current Profiler. USGS, Open-
995 File Report 01-1, <https://pubs.usgs.gov/of/2001/ofr0101/>, 2002.

996

997 Singer, M. B.: A new sampler for extracting bed material sediment from sand and gravel beds in navigable rivers.
998 *Earth Surface Processes and Landforms* 33(14):2277 – 2284 DOI: 10.1002/esp.1661, 2008.

999

1000 Soloy, A., Turki, I., Fournier, M., Costa, S., Peuziat, B. and Lecoq, N.: A Deep Learning-Based Method for
1001 Quantifying and Mapping the Grain Size on Pebble Beaches. *Remote Sens.*, 12, 3659, doi:10.3390/rs12213659,
1002 2020.

1003

1004 Staudt, F., Mullarney, J. C., Pilditch, C. A. and Huhn, K.: Effects of grain-size distribution and shape on sediment
1005 bed stability, near-bed flow and bed microstructure. *Earth Surface Processes and Landforms*, 44(5). DOI:
1006 10.1002/esp.4559, 2018.

1007

1008 Sun, Z., Zheng, H. and Sun, L.: Analysis on the Characteristics of Bed Materials in the Jinghong Reservoir on the
1009 Lancang River. *Sustainability*, 13, 6874. <https://doi.org/10.3390/su13126874>, 2021.

1010

1011 Takechi, H., Aragaki, S. and Irie, M.: Differentiation of River Sediments Fractions in UAV Aerial Images by
1012 Convolution Neural Network. *Remote Sens.*, 13, 3188. <https://doi.org/10.3390/rs13163188>, 2021.

1013

1014 Taravat, A., Wagner, M. P., Bonifacio, R. and Petit, D.: Advanced Fully Convolutional Networks for Agricultural
1015 Field Boundary Detection. *Remote Sens.*, 13, 722., 2021.

1016

1017 Török, G. T., Baranya, S. (2017) Morphological Investigation of a Critical Reach of the Upper Hungarian Danube.
1018 *Periodica Polytechnica Civil Engineering*. 61(4), pp. 752–761. <https://doi.org/10.3311/PPci.10530>, 2017.

1019

1020 USDA: Guidelines for Sampling Bed Material. Technical Supplement 13A, 2007.

1021

1022 Vanoni, V. A. and Hwang, L. S.: Relation between Bed Forms and Friction in Streams. *J. Hydraulics Division.*,
1023 93 (3), 121–144. doi:10.1061/JYCEAJ.0001607, 1967.

1024

1025 Verdú, J. M., Batalla, R. J. and Martínez-Casanovas, J. A.: High-resolution grain-size characterisation of gravel
1026 bars using imagery analysis and geo-statistics. *Geomorphology*, 72, 73–93., 2005.

1027

1028 Warrick, J. A., Rubin, D. M., Ruggiero, P., Harney, J. N., Draut, A. E. and Buscombe, D.: Cobble cam: Grain-
1029 size measurements of sand to boulder from digital photographs and autocorrelation analyses. *Earth Surf. Process
1030 Landf.*, 34, 1811–1821. <https://doi.org/10.1002/esp.1877>, 2009.

1031

1032 Wilcock, P. R.: Persistence of armor layers in gravel-bed streams. *Hydrology and Land Surface Studies.*
1033 <https://doi.org/10.1029/2004GL021772>, 2005.

1034

1035 Wolcott, J. F., Church, M.: Strategies for sampling spatially heterogeneous phenomena: The example of river
1036 gravels. *Journal of Sedimentary Research*. v. 61, no. 4, p. 534–543, 1991.

1037

1038 Wolman, M. G.: Method of sampling coarse river bed material. *Trans. Am., Geophysical Union*, 35(6), 951-956.
1039

1040 WMO: Measurement of river sediments: prepared by the Rapporteur on Sediment Transport of the Commission
1041 for Hydrology. Report, World Meteorological Organization - No. 561, Operational hydrology report (OHR)- No.
1042 16, 1981.

1043

1044 Xiao, Y., Li, W., & Yang, S.: Hydrodynamic-sediment transport response to waterway depth in the Three Gorges
1045 Reservoir, China. *Arabian Journal of Geosciences*, 14(775). [https://doi.org/10.1007/s12517-021-07090-
1046 7/Published](https://doi.org/10.1007/s12517-021-07090-7/Published), 2021.

1047

1048 Yang, F., Yi, M., Cai, Y., Blasch, E., Sullivan, N., Sheaff, C., Chen, G. and Ling, H.: Multitask Assessment of
1049 Roads and Vehicles Network (MARVN). *Proceedings Volume 10641, Sensors and Systems for Space
1050 Applications XI*, 106410D, <https://doi.org/10.1117/12.2305972>, 2018.

1051

1052 You, K., Long, M., Wang, J., Jordan M.I.: How Does Learning Rate Decay Help Modern Neural Networks?
1053 <https://doi.org/10.48550/arXiv.1908.01878>, 2019.

1054

1055 Yu, L., Wang, S. and Lai, K.K.: Data Preparation in Neural Network Data Analysis. In book: *Foreign-Exchange-
1056 Rate Forecasting with Artificial Neural Networks*. DOI: 10.1007/978-0-387-71720-3_3, 2007.

1057

1058 Zamir, A. R., Sax, A., Shen, W., Guibas, L., Malik, J. and Savarese, S.: Taskonomy: Disentangling Task Transfer
1059 Learning. In *Proceedings of the 2018 IEEE/CVF Conf. on Computer Vision and Pattern Recognition*, Salt Lake
1060 City, UT, USA, pp. 3712–3722. doi: 10.1109/CVPR.2018.00391, 2018.

1061

1062 Zhang, Q., Shi, Y., Chen, Z. and Jiang, T.: ADCP measured flow current of the middle-lower Changjiang River
1063 channel. *Front. Earth Sci., China* 2, 1–9. <https://doi.org/10.1007/s11707-008-0016-y>, 2008.

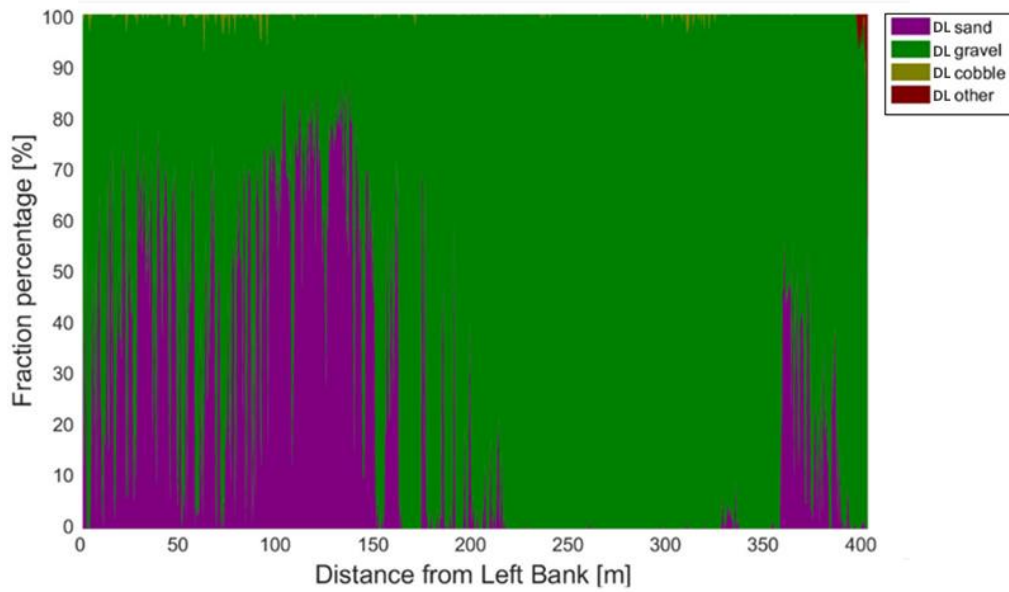
1064
1065
1066
1067
1068
1069
1070
1071

Zhou, Y., Lu, J., Jin, Z., Li, Y., Gao, Y., Liu, Y. and Chen, P.: Experimental Study on the Riverbed Coarsening Process and Changes in the Flow Structure and Resistance in the Gravel Riverbed Downstream of Dams. *Front. Environ. Sci.*, <https://doi.org/10.3389/fenvs.2021.611668>, 2021.

Zhu, J., Park, T., Isola, P. and Efros, A. A.: Unpaired Image-to-Image Translation using Cycle-Consistent Adversarial Networks. arxiv, <https://arxiv.org/abs/1703.10593>, 2020.

1072 Appendix

1073 Appendix A Site A - Section A – II



1074
1075
1076
1077

Figure A1: The sediment fraction percentage results of every image, analysed by the DL algorithm along Section A - II. While the trends are apparent, the sensitivity of the method at its current state can be observed. DL result before applying moving-averaging.

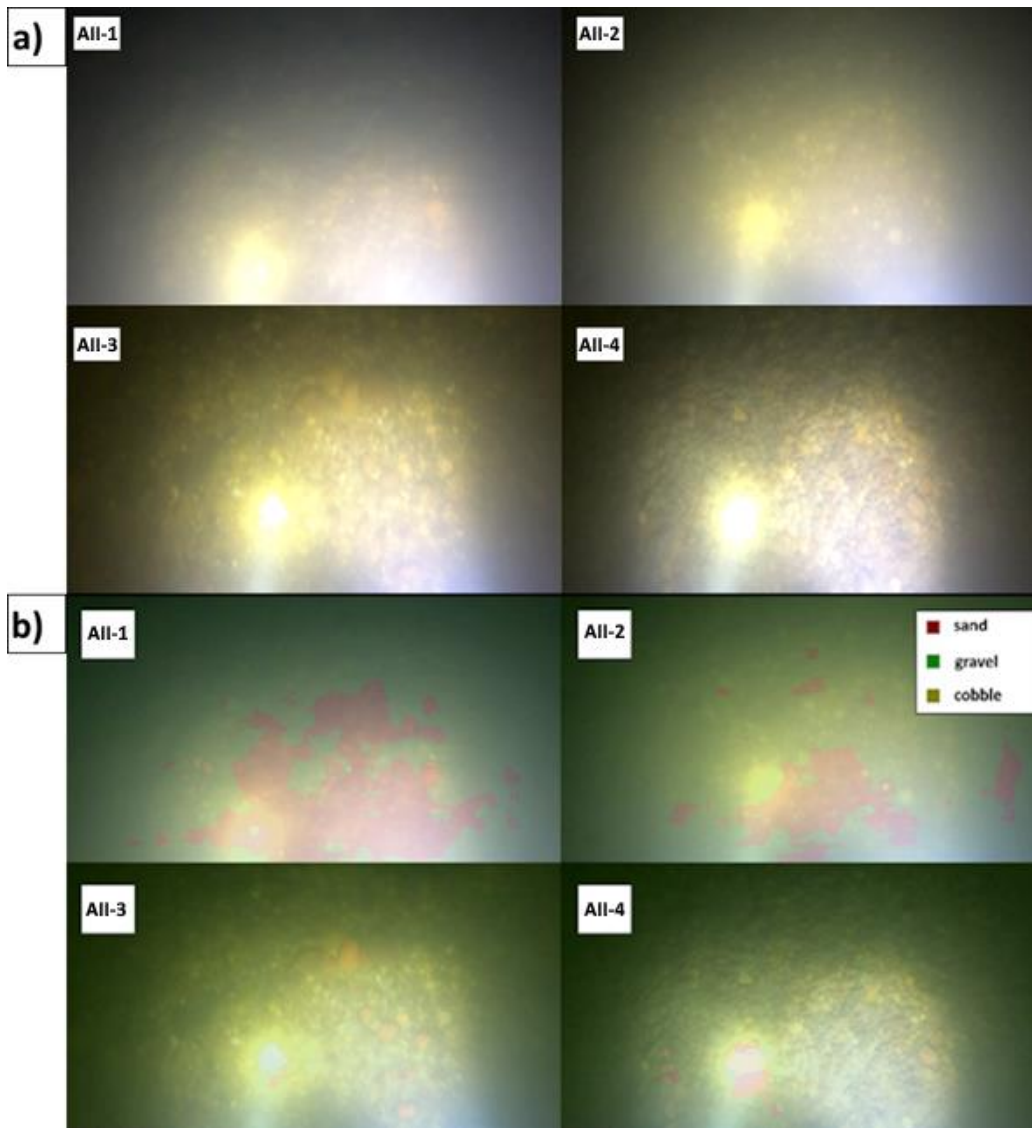
1078



1079
1080
1081

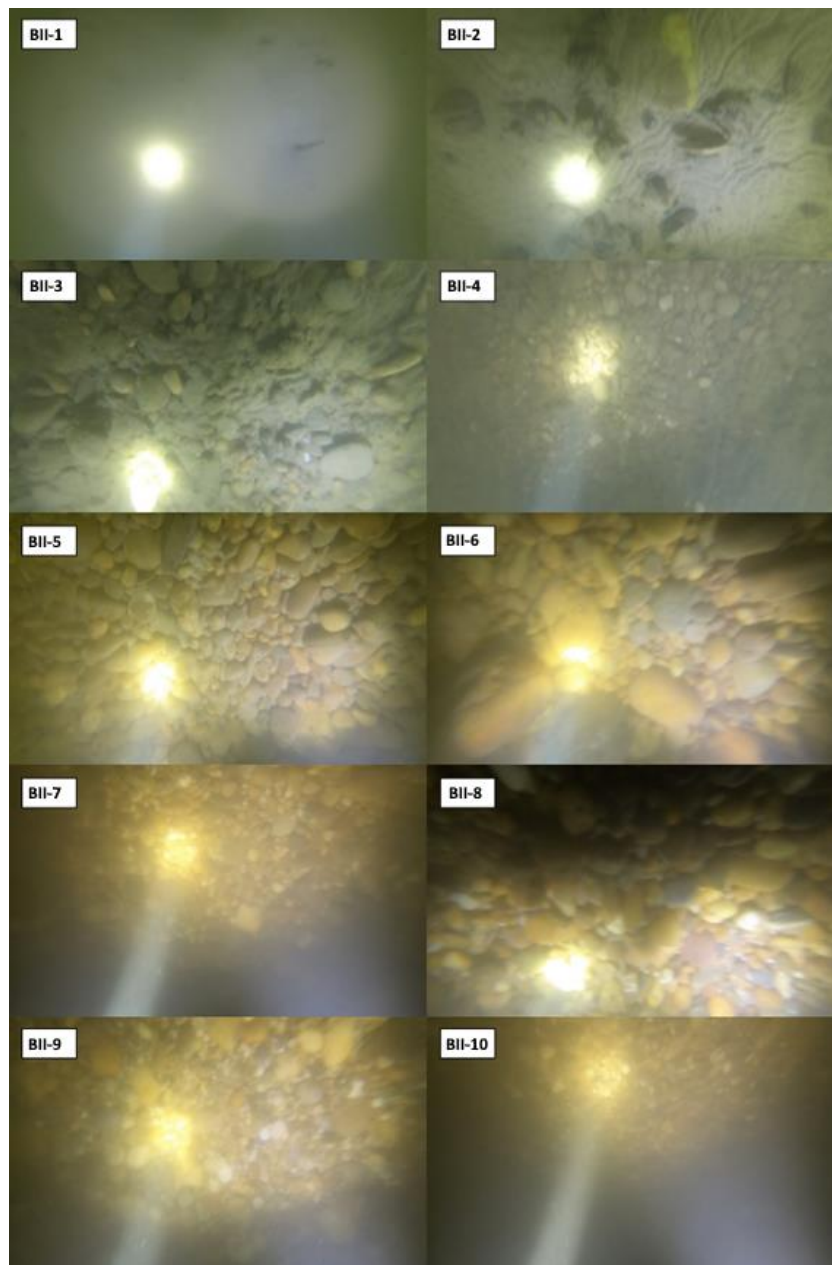
Figure A2: Images of bed armouring, taken during our surveys in the Upper section of the Hungarian Danube. We broke the surface armour to showcase the presence of the underlying finer fractions.

1082

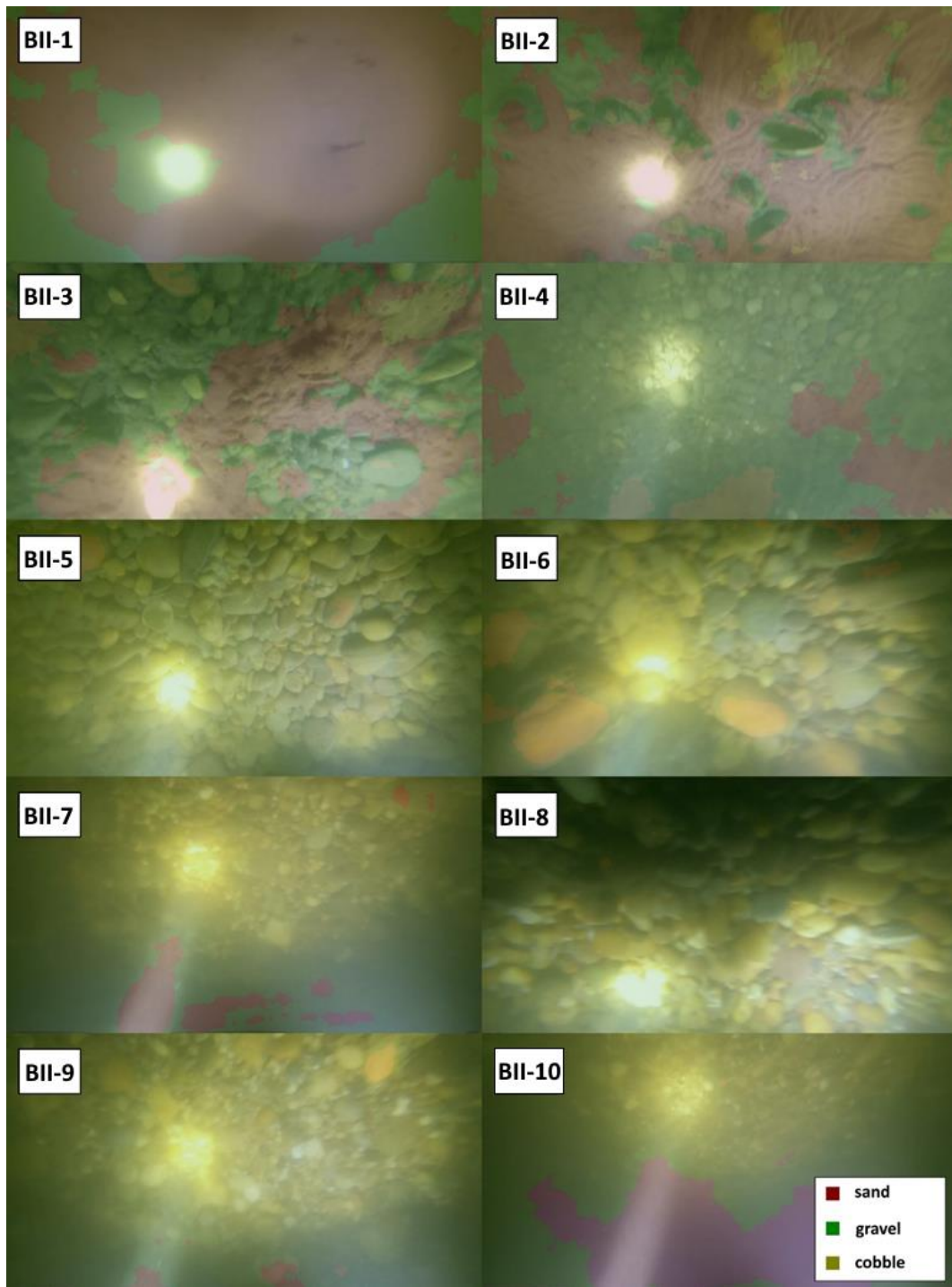


1083
 1084
 1085

Figure A3: a) Riverbed video images at the sampling points in Section A - II. b) Riverbed video images overlapped with their raw, DL detection result, at the sampling points in Section A - II.



1087
1088 Figure B1: Riverbed video images at the sampling points in Section B - II.
1089



1090

1091

1092

1093

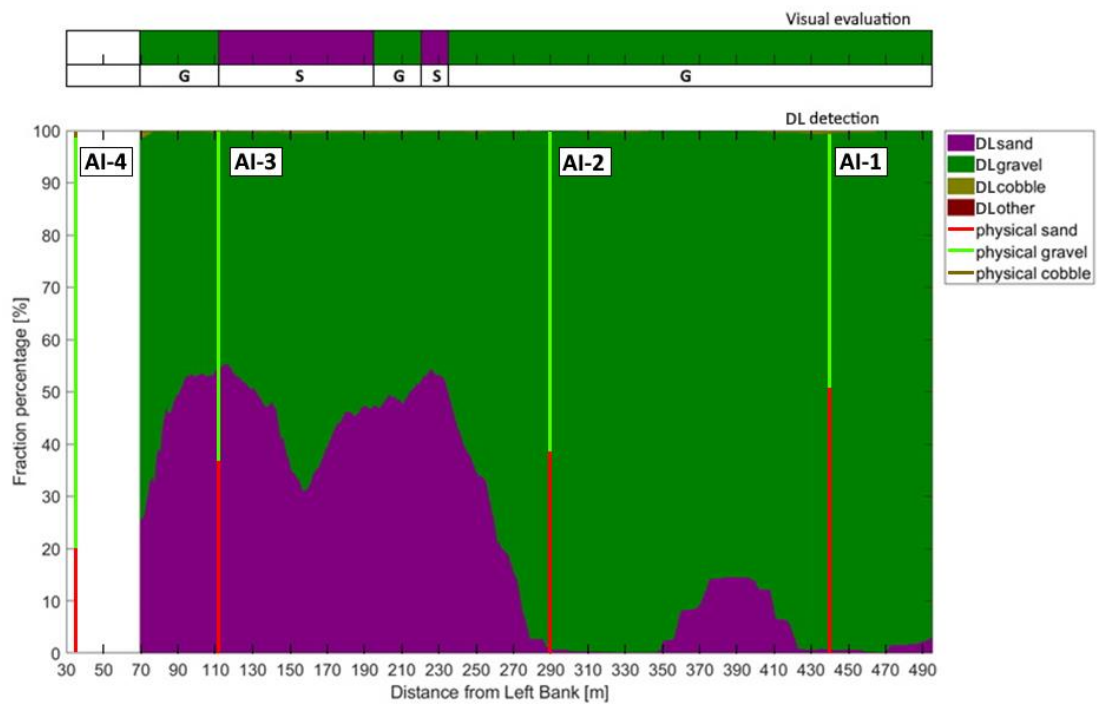
Figure B2: Riverbed video images overlapped with their raw, DL detection result, at the sampling points in Section B - II.

1094 Appendix C Site A - Section A - I



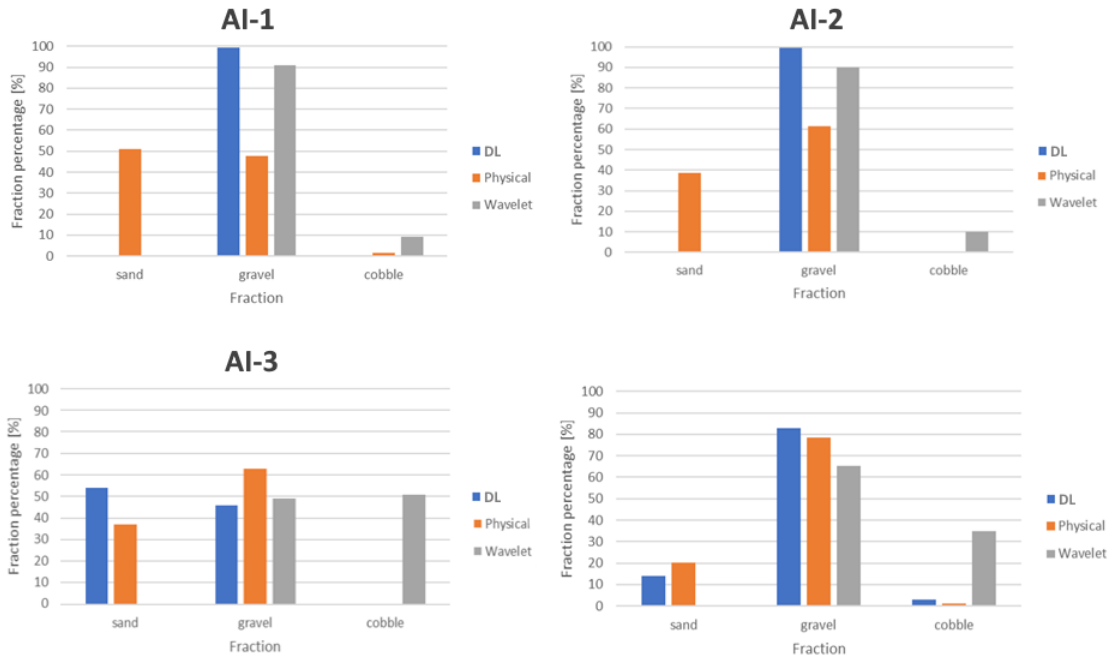
1095 Figure C1: The path of the vessel and camera in Section A - I, Site A. The polyline is coloured based on the sediment
 1096 seen during visual evaluation of the video. Yellow markers are the locations of physical bed material samplings. (Map
 1097 created with Google Earth Pro)
 1098

1099



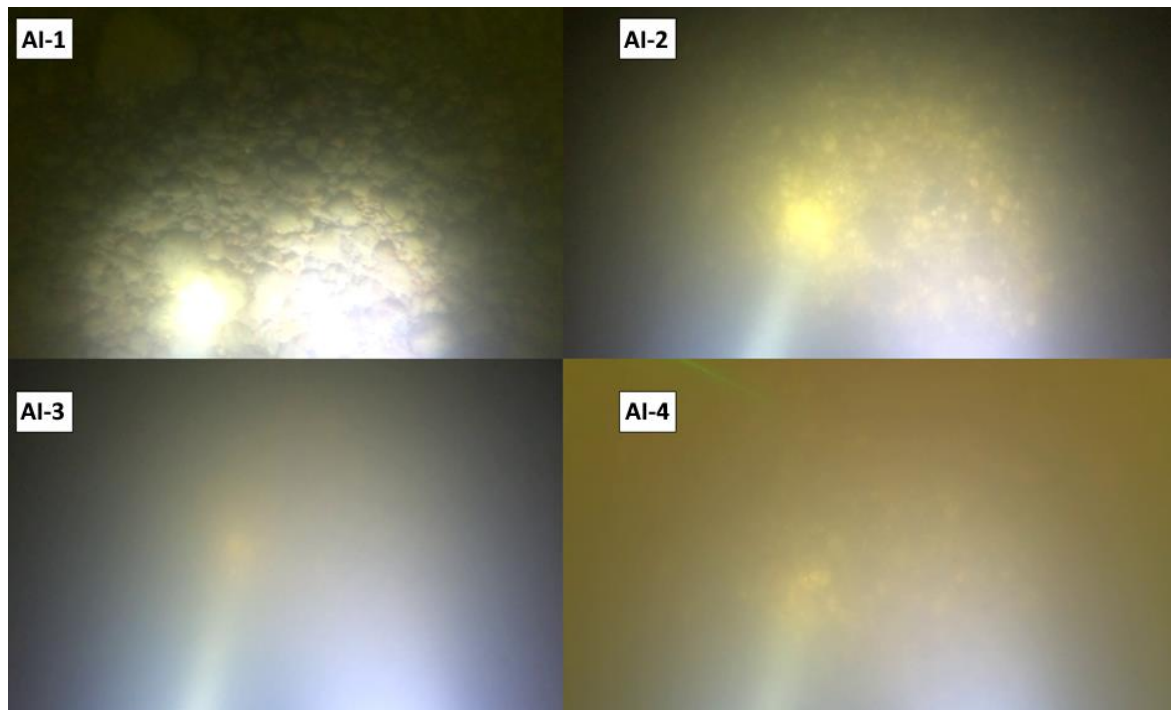
1100 Figure C2: Sediment fraction percentages in Section A - I, recognised by the AI. The visual evaluation included two
 1101 classes: gravel – G, sand – S). The fractions of the physical samples are shown as verticals.
 1102

1103



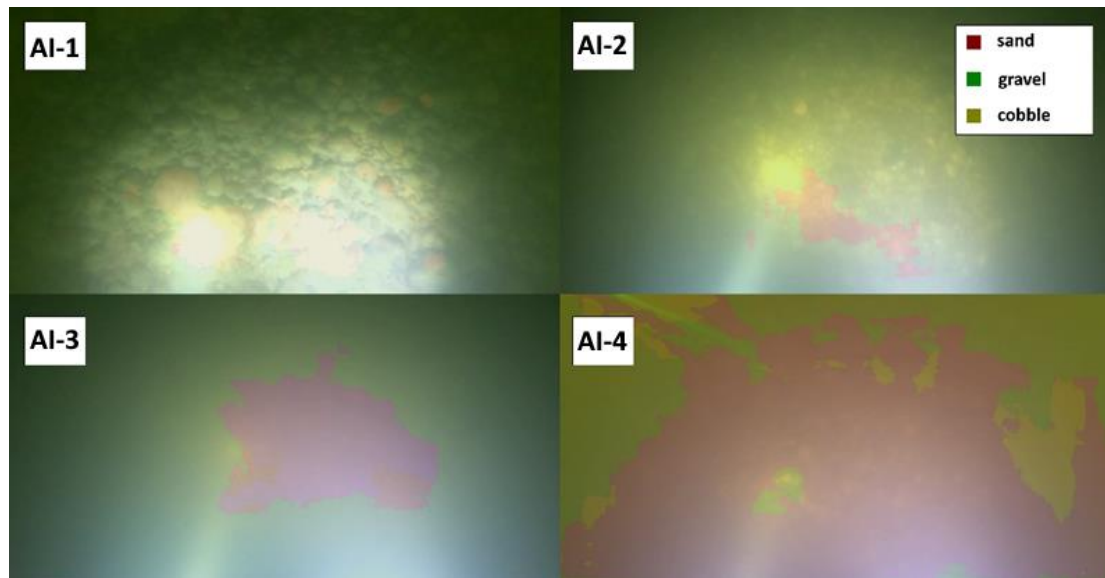
1104
1105
1106

Figure C3: Comparison of sediment fraction % at the sampling locations from the moving-averaged DL detection, conventional sieving and the wavelet-based image processing method. Section A - I.



1107
1108
1109

Figure C4: Riverbed video images at the sampling points in Section A - I.



1110

1111

1112

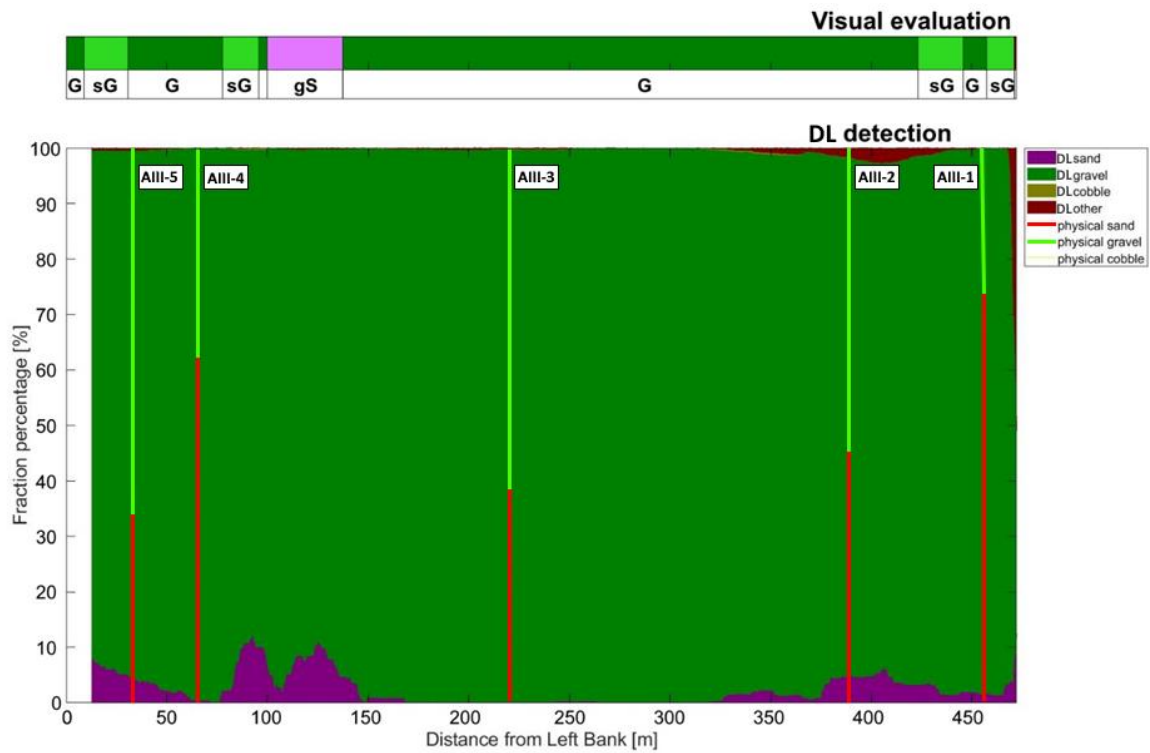
Figure C5: Riverbed video images overlapped with their raw, DL detection result, at the sampling points in Section A-I.

1113 Appendix D Site A – Section A - III

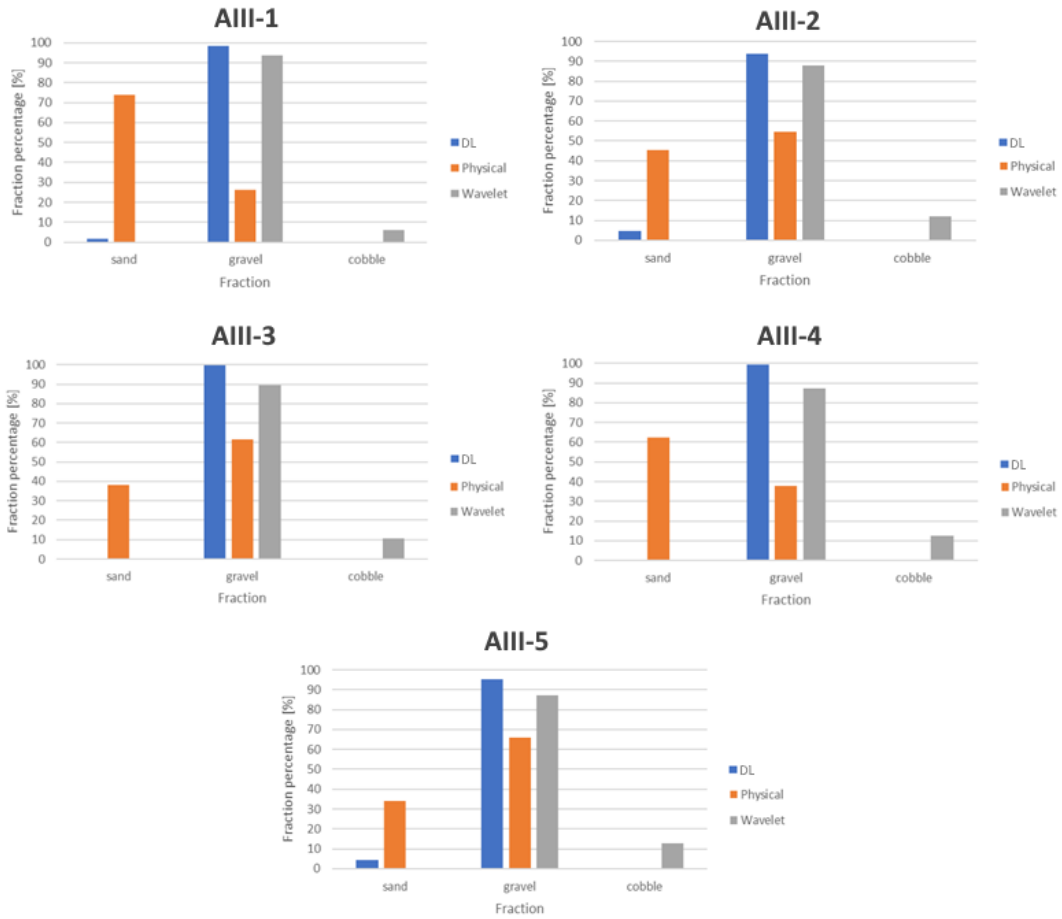


1114 Figure D1: The path of the vessel and camera in Section A - III, Site A. The polyline is coloured based on the sediment
 1115 seen during visual evaluation of the video. Yellow markers are the locations of physical bed material samplings. (Map
 1116 created with Google Earth Pro)
 1117

1118

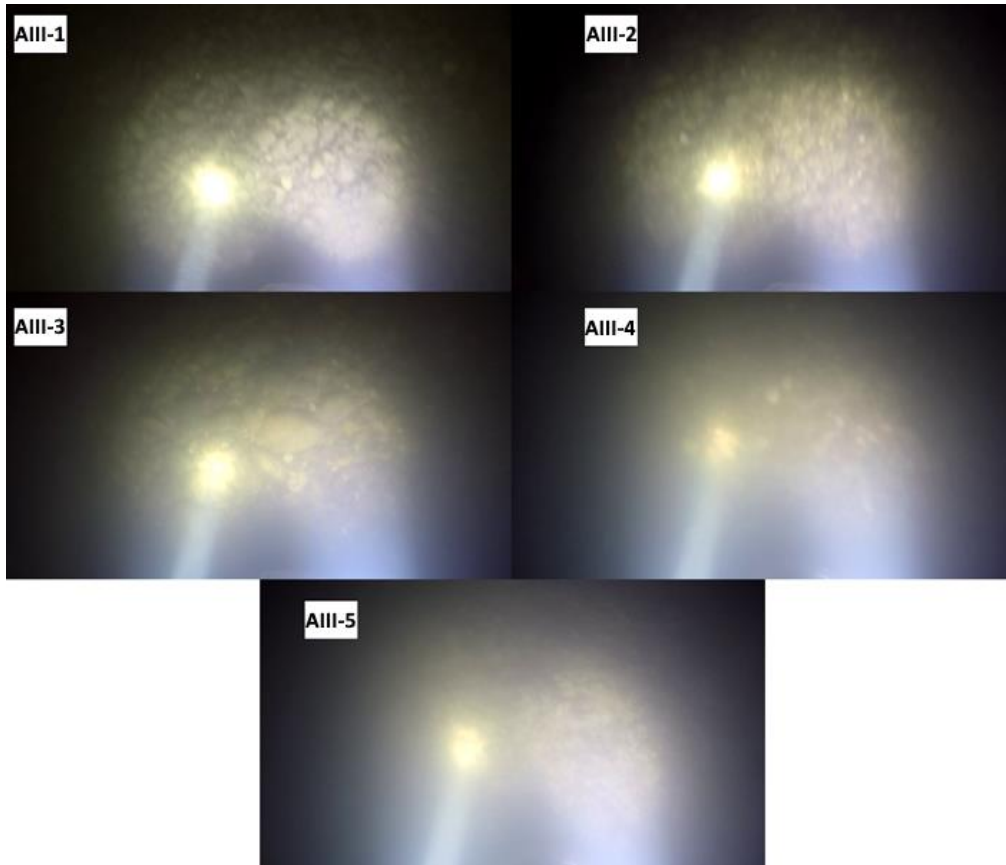


1119 Figure D2: Sediment fraction percentages in Section A - III, recognised by the AI. The visual evaluation included three
 1120 classes: gravel – G, sandy gravel – sG, gravelly sand - gS). The fractions of the physical samples are shown as verticals.
 1121



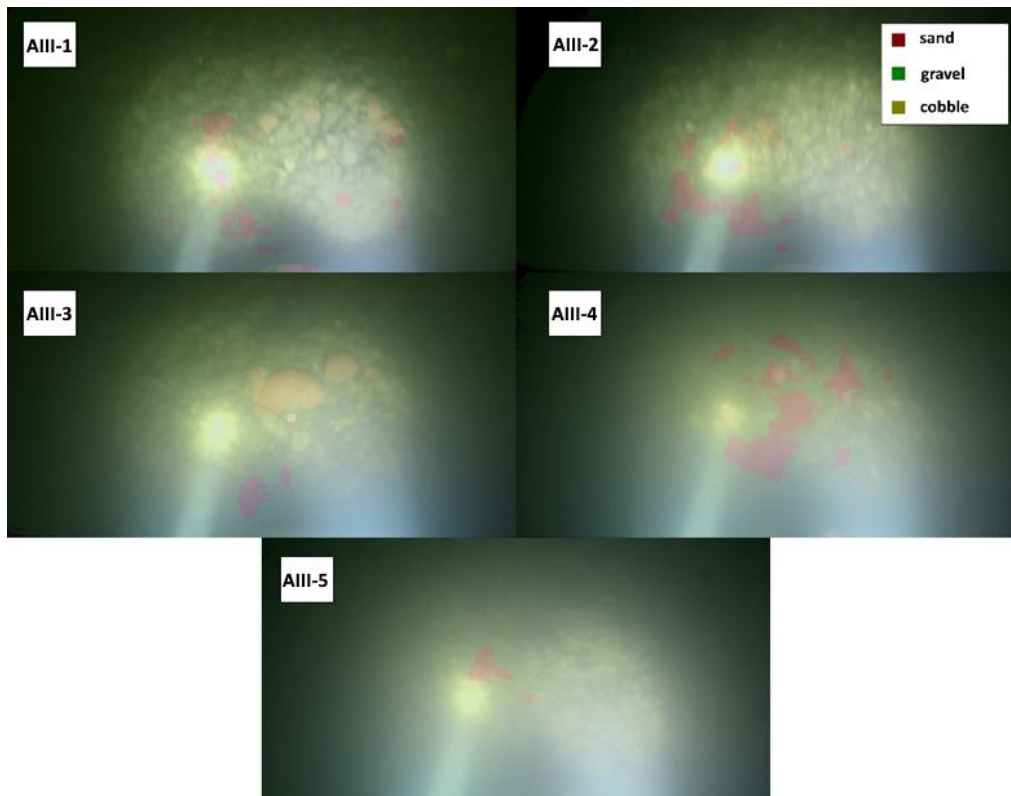
1122
1123
1124

Figure D3: Comparison of sediment fraction % at the sampling locations from the moving-averaged DL detection, conventional sieving and the wavelet-based image processing method. Section A - III.



1125
1126 Figure D4: Riverbed video images at the sampling points in Section A - III.

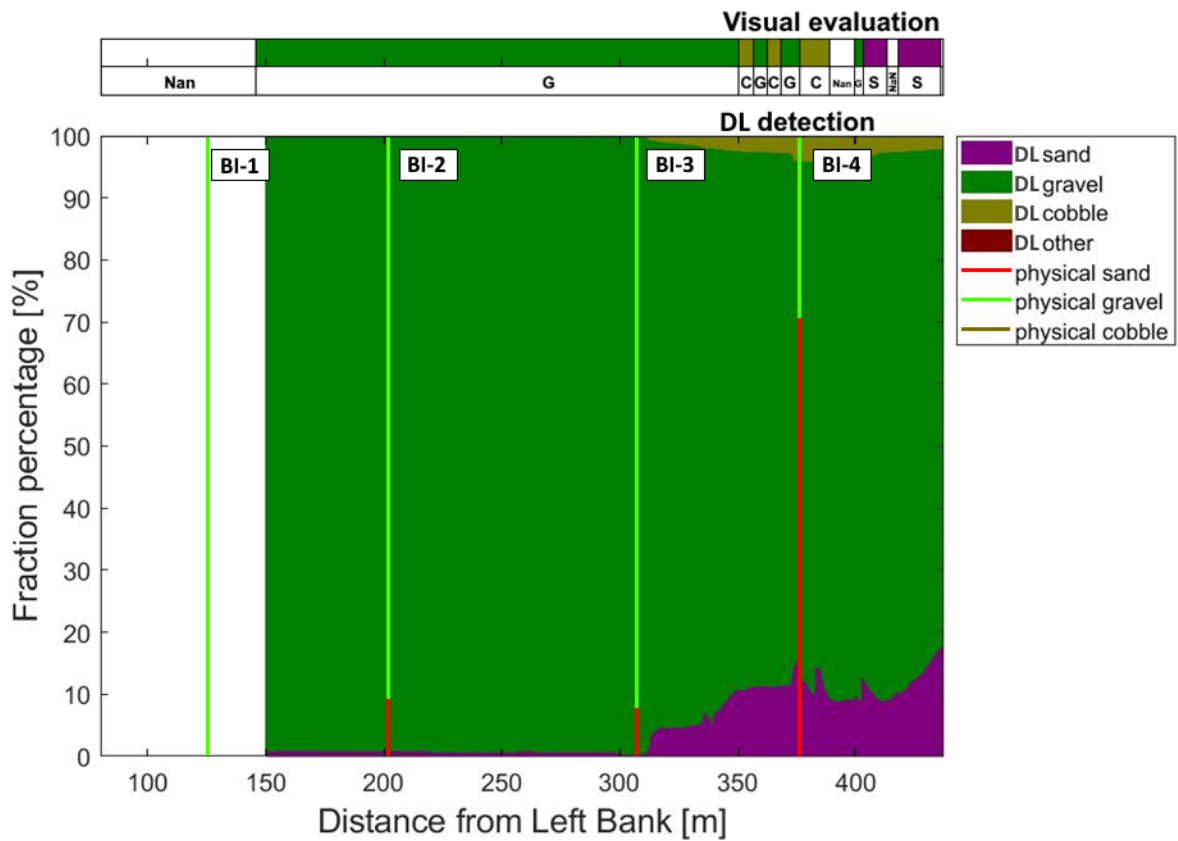
1127



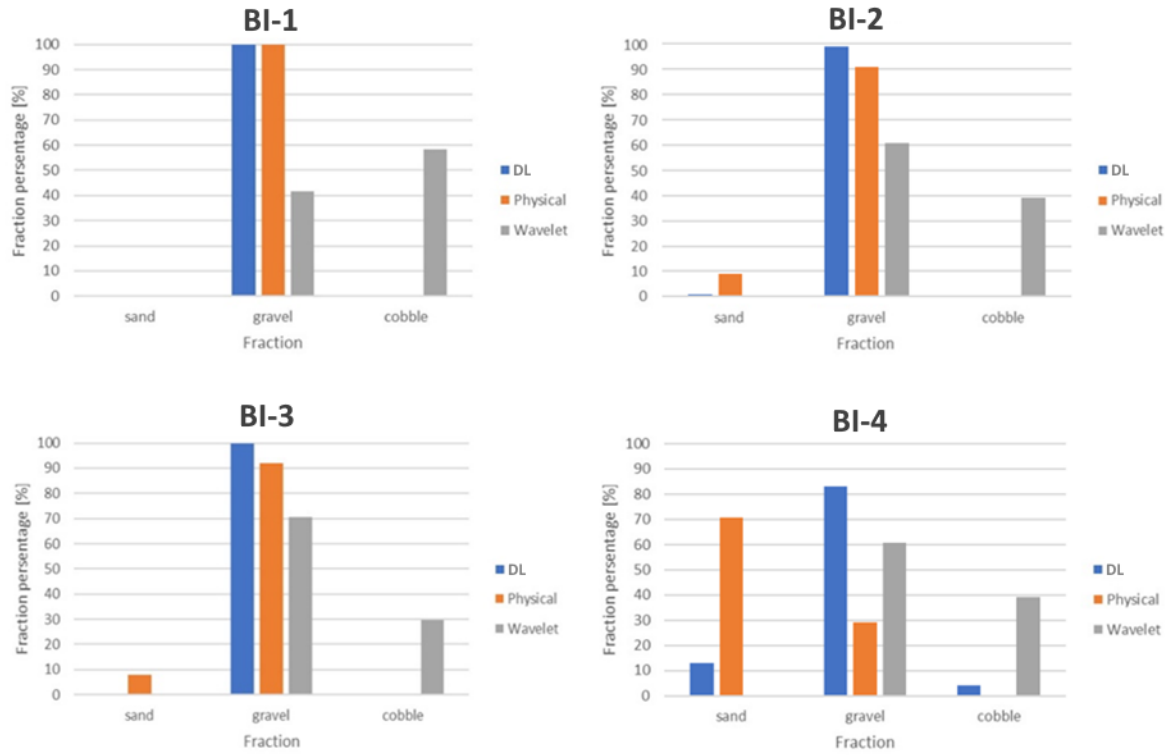
1128
1129 Figure D5: Riverbed video images overlapped with their raw, DL detection result, at the sampling points in Section A
1130 - III.
1131



1133 Figure E1: The path of the vessel and camera in Section B - I, Site B. The polyline is coloured based on the sediment
 1134 seen during visual evaluation of the video. Yellow markers are the locations of physical bed material samplings. (Map
 1135 created with Google Earth Pro)
 1136

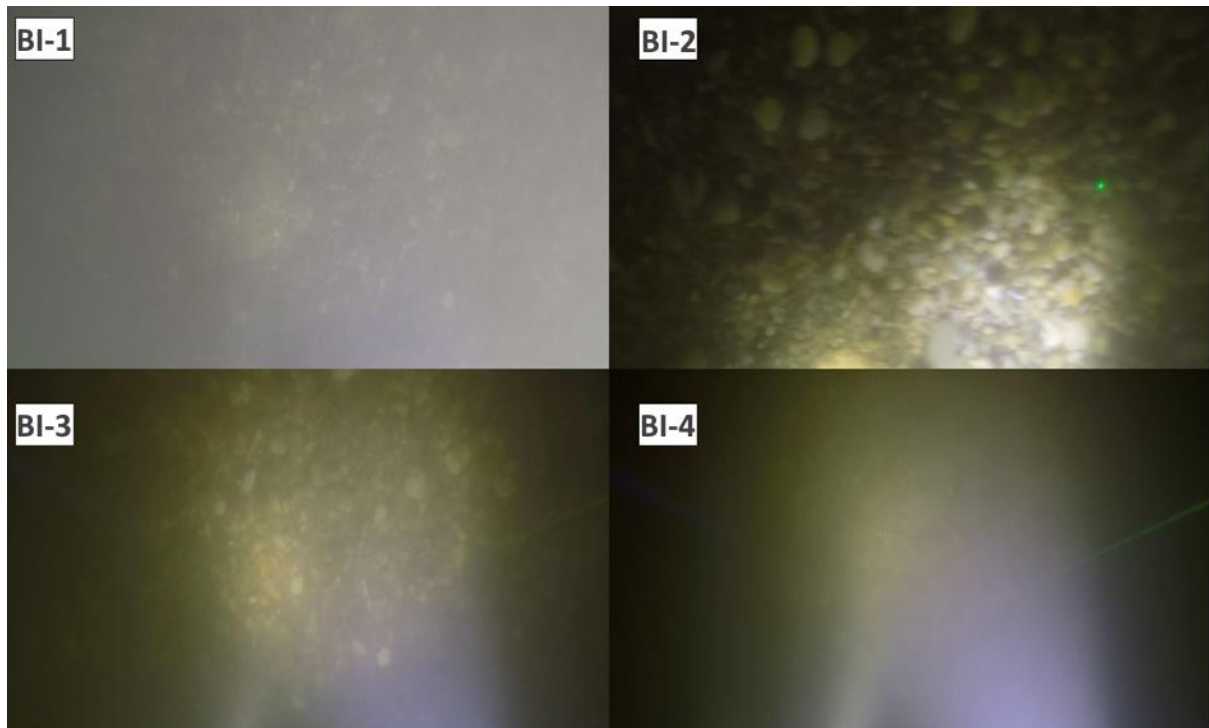


1137 Figure E2: Sediment fraction percentages in Section B - I, recognised by the AI. The visual evaluation included two
 1138 classes: gravel – G, sand – S). The fractions of the physical samples are shown as verticals.
 1139



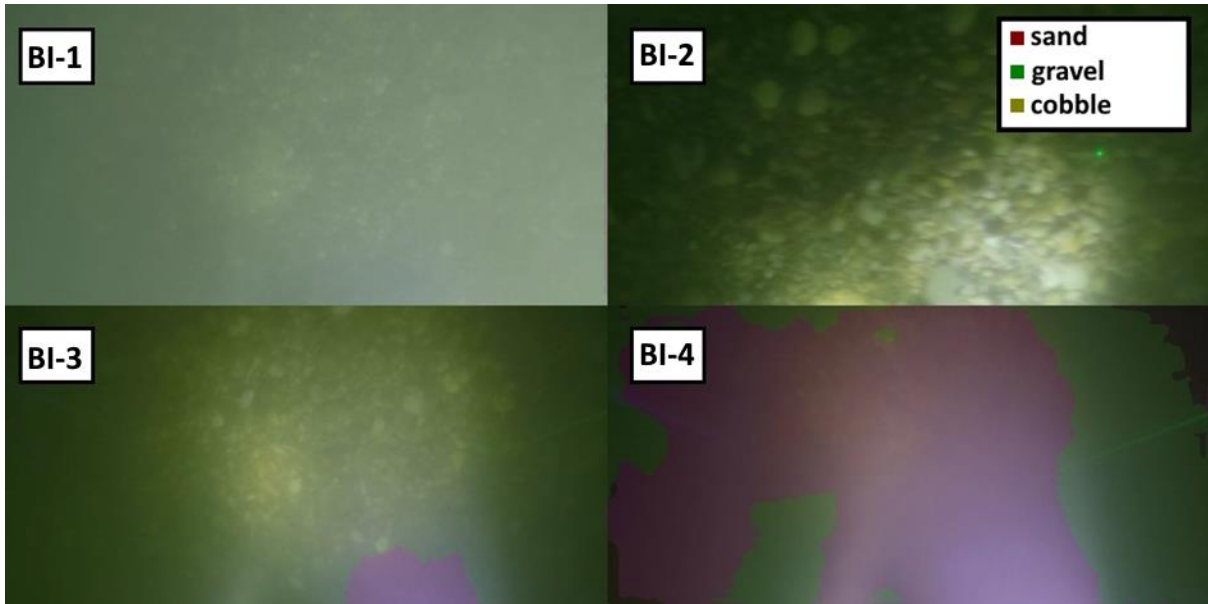
1140
1141
1142

Figure E3: Comparison of sediment fraction % at the sampling locations from the moving-averaged DL detection, conventional sieving and the wavelet-based image processing method. Section B - I.



1143
1144
1145

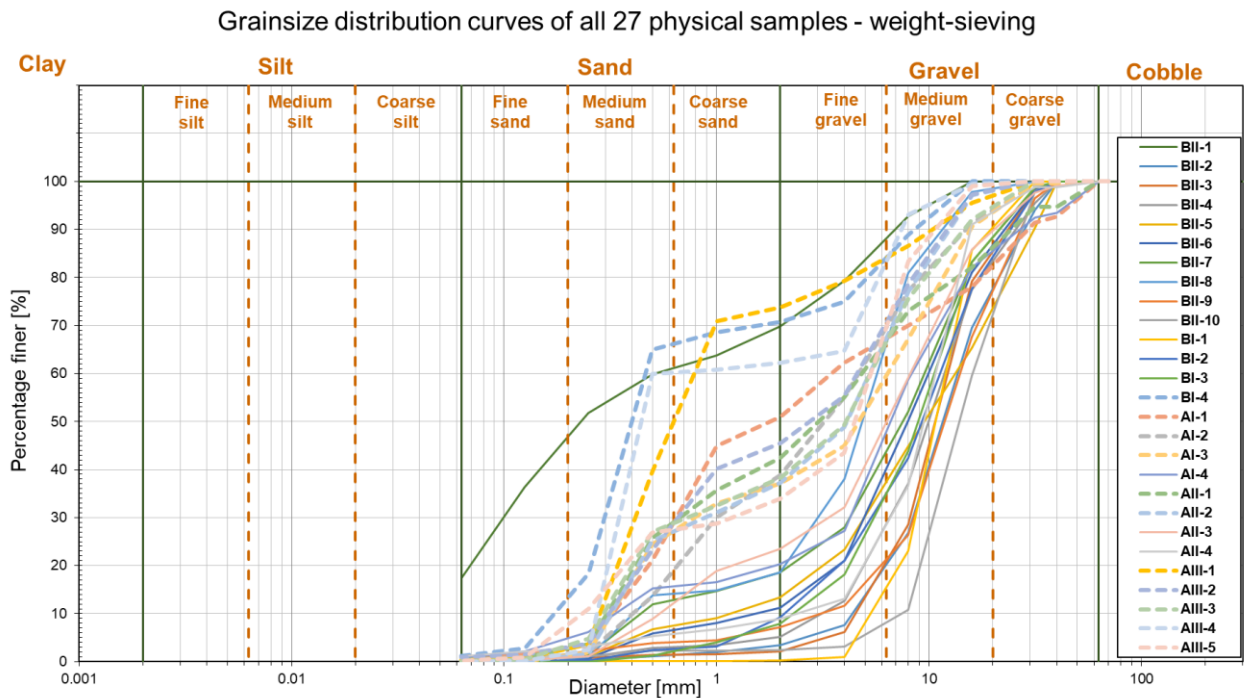
Figure E4: Riverbed video images at the sampling points in Section B - I.



1146
1147 Figure E5: Riverbed video images overlapped with their raw, DL detection result, at the sampling points in Section B
1148 - I.

1149

1150 Appendix F



1151
1152 Figure F1: Grainsize distribution curves of the 27 sieved physical samples. 11 curves categorised as Outlier Type-A are
1153 showcased with dashed lines. The shapes of these curves are representing bimodal (gap graded) sediment distributions,
1154 which typically refers to bed armouring (i.e., excess of a certain particle size, a coarser surface layer protects a finer
1155 subsurface layer from being washed away). Hence, analysing images of the surface layer could not represent these
1156 complex distributions inherently.